Master Thesis

Elasticity and Vacancy Behaviour of Crystals of Hard Cubes

Author:
Mayke Ploeger

Supervisor:
Dr. Laura Filion

Utrecht, The Netherlands

January 30, 2017

Utrecht University

Master Program in Nanomaterials:
Chemistry and Physics
Debeye Institute
Utrecht University

Abstract

In this thesis we examine the effects of vacancies on the elasticity of a simple cubic crystal with cubic particles. We calculate the elastic constants as a function of the vacancy concentration and the packing fraction. Furthermore we examine the correlation between the deformation of the crystal and the direction of the defects caused by vacancies in the crystal, for a shear and a stretch deformation. To this extent we explore two viable simulation techniques: the Monte Carlo and the Event Driven Molecular Dynamics methods. We implement two different methods of calculating the elastic constants in the two respective simulations: calculation by means of global strain fluctuations and calculation by means of the stress-strain relation. We find that for a stable crystal, the elastic constants C_{11} and C_{44} increase as a function of both the packing fraction and the vacancy concentration, while C_{12} decreases. Furthermore we find that there is no correlation between a shear deformation and the direction of the defects. For the stretch deformation, the defects align with the compressed direction.

Contents

Chapter 1

Introduction

The Dee bridge' collapse in 1847 was one of the first architectural disasters which instigated a formal inquiry into a structural failure. The Dee bridge was followed by the Tay Rail Bridge disaster in 1879. Repeating failures of other dynamically loaded constructions started the systematic investigation of fracture and fatigue. In the first half of the twentieth century, the research was dominated by empirical and mechanical views on fracture, that were based on results from experiments that applied linear elastic fracture mechanics [1]. The failure or success of structural materials was believed to depend mainly on their chemical composition, a macroscopic property. More fundamental research resulted in the insight that the microscopic structure plays a large role in the resistance of materials to fracture, and thus in the "elasticity" of materials. Around 1950, material science started to rely more and more on physics, chemistry, and mechanical engineering, and on the theory on the elastic response of materials.

Physicists have been interested in elasticity for much longer. Galilei investigated the resistance of solids to fracture in 1638 already [2]. Specifically, he looked at a beam of which one end is built into a wall. The beam will bend when its own weight is large enough or when it is subjected to a large enough force. Although Galilei was not aware of the elasticity of solids, his investigation was the start of the development of the theory of elasticity. The first great discovery in this field was made by Hooke in 1660 - published in 1678 [2] . Hooke's famous law states that the force needed to stretch or compress a "springy body" by a distance x is proportional to that same distance. The generalized form of this law forms the basis of the theory of elasticity. Hooke did not address Galilei's problem. The first important investigation related to the problem of the beam was by Bernoulli in 1705 [2]. He assumed that the resistance to the bending of a thin rod emerges from the expansion and compression of the "inner fibers" of the rod. Thus Bernoulli thought that the inner structure of the rod changes during bending.

We now know that the inner structure indeed changes, as the vectors between the positions of the particles that make up the structure change in direction and/or length [3]. What Bernoulli called the expansion or compression of fibers is actually the rearrangement of the particles due to the force on Galilei's beam. If the change due to this rearrangement is small enough, the beam will return to its original shape when the force on the beam disappears. That happens because the beam is "elastic." Elastic structures will return to their equilibrium shape after small enough deformations when the cause of the deformation is removed. Very elastic objects, such as a bouncy ball, can be subjected to large forces, and still return to their original shape after the removal of these forces. The force needed to deform objects is smaller for the more elastic objects (like the bouncy ball) than the stiffer ones (the beam). The difference in elasticity between the bouncy ball and the metallic beam arises due to their microscopic structure. The structure of the metallic beam depends on inter-atomic interactions, whereas the bouncy ball's structure is made up of polymers, a type of colloid, which interact quite differently than atoms.

A colloid is a particle that is substantially larger than an atom, but is small enough to exhibit Brownian motion. Typically, a particle is a colloid if its size is between 10 and 1000 nm in at least one dimension. This gives a very broad variety of particles that fit this definition. The most general colloids are rods, platelets, and spheres, which fit the definition in 1, 2, or 3 dimensions. The field of colloid science was once described as "The World of Neglected Dimensions" by Ostwald in 1922 [4]. A few decades have passed since, and while experiments became much more advanced, the rapid development of computer systems and their efficiency

supported the advancement of numerical methods as well. This made room for progressive theoretical models on all length scales, including the neglected one.

The focus of this thesis will lie on a fairly simple type of colloid: the hard particle. Hard particles interact with the hard potential:

$$\psi(r) = \begin{cases} \infty & r < \sigma, \\ 0 & r \geq \sigma, \end{cases} \tag{1.0.1}$$

where σ is the interaction length of the particle, which is equal to the radius for spherical particles. These particles therefore only interact when they collide: as long as the particles do not touch each other, they do not interact. The model is based on high density systems, at which the steep repulsive part of the pair potential dominates. When the repulsion rises to several k_BT over a distance small compared to the size of the particle, the actual potential gets very close to the hard sphere potential. In experiments, the difference will become nearly indistinguishable [5]. The hard particle model is certainly not a good model for all systems, as some systems have a large attractive part as well. There do exist real systems that can well be modelled as a hard sphere system though. Multiple publications show that the dispersion of silica particles can be modelled as a hard sphere fluid [5, 6, 7].

Fortunately, due to recent advancement in synthesis techniques, the syntheses of a wider variety of shapes of particles has been made possible. There are many applications in which the shape of the particle is an important characteristic. For instance, in drug delivery [8], or optics [9]. That is why, with the possibility to create more shapes, the study of the theory of those new particles expanded as well. Torquato and Stilinger described the close packing of many anisotropic particles [10]. One of those interesting new shapes is the cube, naturally found in the minerals galena, pyrite and fluorite. In 2010, Rossi et al. found that their cubic colloids formed simple cubic crystals [11]. This is one of the exiting differences with respect to spherical particles: for spherical particles, the simple cubic structure is almost always unstable. Polonium is the only known single atomic crystal that is an exception to this rule [12]. There might exist other differences with respect to the crystals of spherical particles as well.

Since Rossi, extensive computational research has been done on the phase behaviour of cubes [13, 14, 15, 16]. The latter paper [16], from Smallenburg, is the foundation of the motivation for this thesis. He found that when vacancies[1] are added to the cubic particle crystal, chain-like defects form at the position of these vacancies, see Fig. 1.0.1. These defects are not found in crystals with spherical particles. Moreover, the ideal vacancy concentration near the melting point for crystals of hard cubes ($v = \frac{\#vacancies}{\#lattice\ sites} = 0.065$ [16]) is two orders higher than that for crystals of hard spheres ($v = 10^{-4}$ [17]). Summarizing, the structure of hard cube crystals differs in at least three points with the structure of hard sphere crystals: it is a simple cubic instead of a face centred cubic crystal; the ideal vacancy concentration of hard cubes is much higher than that of hard spheres; and large chain-like defects are formed at the position of these vacancies, which does not happen for hard spheres.

Earlier, we stated that the microscopic structure has a significant effect on the elasticity. We have now characterized three main structural differences between the hard cube and the hard sphere crystal. We would therefore expect a different behaviour for both crystals under stress. The behaviour of hard spheres has been widely studied [18, 19], but the same has not been done for hard cubes yet. In this thesis, we will study the elasticity of hard cube crystals and the correlation between vacancies in a crystal and the elasticity.

[1] A vacancy is a point defect in a crystal lattice where a particle is missing. As a result the number of lattice sites is higher than the number of particles.

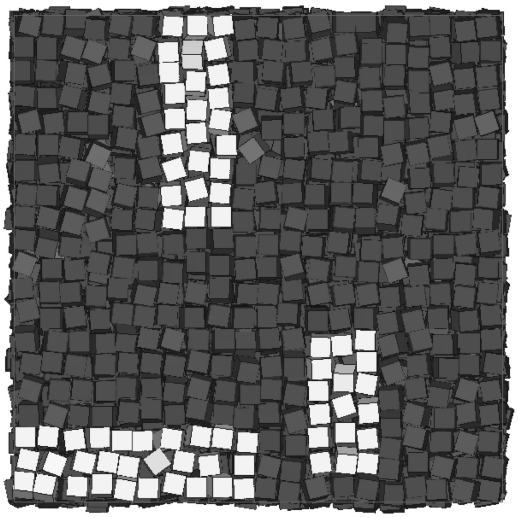

Figure 1.0.1: A snapshot of a crystal with a vacancy concentration of $v = 0.016$. Three chain-like defects and their neighbouring particles are highlighted. In the uppermost defect, six particles share seven lattice sites. In the leftmost defect, seven particles share eight lattice sites. In the rightmost defect, three particles share four lattice sites (taken from Ref. [16]).

1.1 Thesis Outline

In this thesis we study the elastic constants of the hard cube system. In the second chapter, we discuss the theory of elasticity. We introduce the necessary concepts needed in the calculation of the elastic modulus tensor. Then we describe two methods of calculating the relevant elastic constants and discuss two simulation techniques: Monte Carlo and Event Driven Molecular Dynamics simulations. The third chapter discusses the implementation of the calculation in the two computer simulations. The fourth and fifth chapter discuss the results that we found. First, we check the hard sphere system for consistency between the two methods. Subsequently, we calculate the elastic constants of the hard cube system at various packing fractions and vacancy concentrations. Next, we track the direction of the defects caused by vacancies for different non-linear deformations of the crystal. We conclude this thesis with a discussion of the results, and an outlook for further research.

Chapter 2

Theory

In this chapter we describe the theory associated with elastic constants. We describe what they are and introduce the concepts needed in defining and calculating the elastic constants: the strain tensor, the stress tensor and the bulk modulus. Moreover we discuss the theory we need in order to be able to use these concepts to calculate the elastic constants. We conclude this chapter with a theoretical discussion of two simulation techniques: Monte Carlo and Event Driven Molecular Dynamics simulations.

2.1 Elastic Constants

Elastic constants are used to quantize the reaction of a system to a deformation. Solid substances have non-zero elastic constants, while liquids and gases do not have a body to deform and therefore their elastic constants are equal to zero. When deforming a solid body, the position of any point in the body is displaced. This displacement can be described by the displacement vector $\vec{u} = \vec{r}' - \vec{r}$, where $\vec{r} = (x_1, x_2, x_3)$ is the original vector and $\vec{r}' = (x_1', x_2', x_3')$ the vector of the displaced point. Because the position of any point in the body is displaced, the distance between any two points changes as well, as shown in Fig. 2.1.1. The change in an element of length caused by a deformation is described by the strain tensor. In the next section, we will derive the strain tensor from the displacement vector.

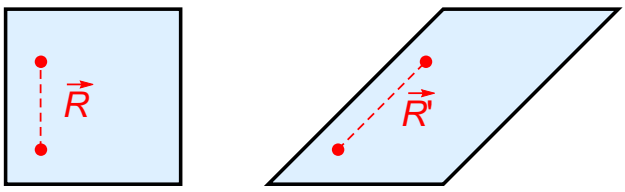

Figure 2.1.1: The parallelogram on the right is the deformed (in this case sheared) version of the square on the left. The two red points are displaced as a result of the deformation. Consequently, the vector $\vec{R}$ between the two indicated points in the square is deformed to the vector $\vec{R}'$ in the parallelogram.

2.1.1 Strain Tensor

Consider two points $\vec{r_1}$ and $\vec{r_2}$ that are very close to each other and define $\mathrm{d}\vec{r} = \vec{r_2} - \vec{r_1}$. When a small deformation is applied, we expect the new positions of $\vec{r_1}$ and $\vec{r_2}$ (denoted $\vec{r_1}'$ and $\vec{r_2}'$) to be close to each other. Let $\mathrm{d}\vec{r}'$ be the new vector joining $\vec{r_1}'$ and $\vec{r_2}'$. Then [3]:

$$\mathrm{d}\vec{r}' = \vec{r_2}' - \vec{r_1}' = \vec{u_2} + \vec{r_2} - (\vec{u_1} + \vec{r_1}) = \mathrm{d}\vec{r} + \mathrm{d}\vec{u}.$$

From this we can calculate the squared length of the old and the new vectors. We define the lengths $\mathrm{d}l^2 \equiv \mathrm{d}x_i^2$ and $\mathrm{d}l'^2 \equiv \mathrm{d}x_i'^2 = (\mathrm{d}x_i + \mathrm{d}u_i)^2$, where the Einstein notation is applied.[1] Using $\mathrm{d}u_i = (\partial u_i/\partial x_j)\mathrm{d}x_j$, $\mathrm{d}l'^2$ can

[1] The convention of the Einstein notation is such that when an index appears twice in a single term, the term should be summed over every possible value of that index: $a_i b_i \equiv \sum_{i=1}^{i_{\max}} a_i b_i$.

be rewritten as:

$$\mathrm{d}l'^2 = \mathrm{d}l^2 + 2\frac{\partial u_i}{\partial x_j}\mathrm{d}x_i\mathrm{d}x_j + \frac{\partial u_i}{\partial x_j}\frac{\partial u_i}{\partial x_k}\mathrm{d}x_j\mathrm{d}x_k. \tag{2.1.1}$$

The second term on the right can be rewritten in the symmetrical form:

$$2\frac{\partial u_i}{\partial x_j}\mathrm{d}x_i\mathrm{d}x_j = \frac{\partial u_i}{\partial x_j}\mathrm{d}x_i\mathrm{d}x_j + \frac{\partial u_i}{\partial x_j}\mathrm{d}x_i\mathrm{d}x_j = \frac{\partial u_i}{\partial x_j}\mathrm{d}x_i\mathrm{d}x_j + \frac{\partial u_j}{\partial x_i}\mathrm{d}x_j\mathrm{d}x_i = \left(\frac{\partial u_i}{\partial x_j} + \frac{\partial u_j}{\partial x_i}\right)\mathrm{d}x_i\mathrm{d}x_j,$$

because the term is summed over both indices i and j, which are thus interchangeable. Now we substitute this symmetric form and swap the indices i and k in the third term of $\mathrm{d}l'^2$ giving:

$$\mathrm{d}l'^2 = \mathrm{d}l^2 + 2\epsilon_{ij}\mathrm{d}x_i\mathrm{d}x_j,$$

where ϵ is the stress tensor and is given by:

$$\epsilon_{ij} = \frac{1}{2}\left(\frac{\partial u_i}{\partial x_j} + \frac{\partial u_j}{\partial x_i} + \frac{\partial u_k}{\partial x_i}\frac{\partial u_k}{\partial x_j}\right). \tag{2.1.2}$$

From its definition it follows that the strain tensor is symmetrical: $\epsilon_{ij} = \epsilon_{ji}$. For reasons that will become clear later, it is convenient to write the strain tensor as a function of the deformation matrix $\mathbf{D}$, which is defined such that $\vec{r'} = \mathbf{D}\cdot\vec{r}$. We can rewrite the strain tensor in terms of $\mathbf{D}$ as follows:

$$\begin{aligned}
x'_i &= D_{ij}x_j,\\
u_i &= x'_i - x_i,\\
\epsilon_{ij} &= \frac{1}{2}\left(D_{ij} - \delta_{ij} + D_{ji} - \delta_{ji} + (D_{ki} - \delta_{ki})(D_{kj} - \delta_{kj})\right),\\
&= \frac{1}{2}\left(D_{ij} + D_{ji} - 2\delta_{ij} + D_{ki}D_{kj} - D_{ji} - D_{ij} + \delta_{ij}\right),\\
&= \frac{1}{2}(D_{ki}D_{kj} - \delta_{ij}),\\
\epsilon &= \frac{1}{2}(\mathbf{D}^T\mathbf{D} - \mathbf{I}).
\end{aligned} \tag{2.1.3}$$

2.1.2 Stress Tensor

When a body is undeformed (i.e. not subjected to strain), it is in a state of thermal equilibrium. That means that any deformation pulls the body out of its equilibrium state. Therefore, internal forces will arise to counter the deformation, such that the body can return to its equilibrium state. These forces are called internal stresses. In this section, we will define the stress tensor, which is related to these forces. Subsequently we will rewrite the stress tensor in terms of the strain tensor and the free energy.

First, we take a closer look at the internal forces. They arise because the atoms or molecules in the body are displaced from their ideal position with respect to each other. The forces are thus inter-molecular forces, which are very short-ranged. They affect only neighbouring molecules, so their reach is approximately equal to the size of a single molecule. The molecular length scale is negligible with respect to the length scale that the theory of elasticity is considered with, which is the macroscopic length scale. This means the following: consider an arbitrary portion A of the body. Because of the range of the internal stresses, the neighbouring portions B_i only act on the surface of the considered portion A. The portions B_i do not have an effect on the interior of portion A, because their range is negligible.

Now consider the total force on portion A. It is equal to the integral of the force per unit volume over the volume of the portion: $\int_{V_A}\vec{F}\mathrm{d}V$. Furthermore, it follows from Newton's third law that any internal forces in portion A cannot contribute to the total force. They must cancel each other. The forces from the surrounding portions B_i can contribute to the total force, but they only act on the surface of portion A, as we established earlier. The volume integral of the total force can thus be rewritten as a surface integral. Note that this is true for any arbitrary portion of the body, as we laid no restrictions on portion A. Gauss' divergence theorem states that a volume integral over a scalar is equal to a surface integral if the scalar is a divergence:

$$\int_V(\nabla\cdot X)\mathrm{d}V = \oint_S(X\cdot n)\mathrm{d}S,$$

or, using the Einstein notation:

$$\int_V \frac{\partial X_i}{\partial x_i} \mathrm{d}V = \oint_S X_i n_i \mathrm{d}S = \oint_S X_i \mathrm{d}s_i, \tag{2.1.4}$$

where n is the normal to the surface directed outward, and s_i are the surface elements directed along the normal. As we do not integrate over a scalar but over the vector $\vec{F}$, we can conclude that $\vec{F}$ must be the divergence of a tensor [3]:

$$F_i = \frac{\partial \sigma_{ij}}{\partial x_j}. \tag{2.1.5}$$

Note that σ is called the stress tensor. The total force on a portion of the body can be rewritten in terms of σ using Gauss' divergence theorem:

$$\int F_i \mathrm{d}V = \int \frac{\partial \sigma_{ij}}{\partial x_j} \mathrm{d}V = \oint \sigma_{ij} \mathrm{d}s_j. \tag{2.1.6}$$

Let us now consider the moment $\vec{F} \times \vec{r}$, with $\vec{r}$ the point where the force is exerted on. The components of the moment are equal to $F_i x_j - F_j x_i$. The moment of the total force on a portion of the body is then equal to $M_{ij} = \int (F_i x_j - F_j x_i) \mathrm{d}V$. For reasons that will become clear later, we rewrite the moment in terms of σ, by substituting Eq. 2.1.5:

$$\begin{aligned} M_{ij} &= \int \left(\frac{\partial \sigma_{ik}}{\partial x_k} x_j - \frac{\partial \sigma_{jk}}{\partial x_k} x_i \right) \mathrm{d}V, \\ &= \int \left(\frac{\partial \sigma_{ik}}{\partial x_k} x_j - \frac{\partial \sigma_{jk}}{\partial x_k} x_i + \sigma_{ij} - \sigma_{ji} - (\sigma_{ij} - \sigma_{ji}) \right) \mathrm{d}V. \end{aligned}$$

For the next step we use the fact that $\delta_{ij} = \frac{\partial x_i}{\partial x_j}$, such that $\sigma_{ij} = \sigma_{ik}\delta_{jk} = \sigma_{ik}\frac{\partial x_j}{\partial x_k}$. This leads to:

$$\begin{aligned} M_{ij} &= \int \left(\frac{\partial \sigma_{ik}}{\partial x_k} x_j - \frac{\partial \sigma_{jk}}{\partial x_k} x_i + \sigma_{ik} \frac{\partial x_j}{\partial x_k} - \sigma_{jk} \frac{\partial x_i}{\partial x_k} \right) \mathrm{d}V - \int (\sigma_{ij} - \sigma_{ji}) \mathrm{d}V, \\ &= \int \left(\frac{\partial (\sigma_{ik} x_j - \sigma_{jk} x_i)}{\partial x_k} \right) \mathrm{d}V - \int (\sigma_{ij} - \sigma_{ji}) \mathrm{d}V, \\ &= \oint (\sigma_{ik} x_j - \sigma_{jk} x_i) \mathrm{d}s_k - \int (\sigma_{ij} - \sigma_{ji}) \mathrm{d}V. \end{aligned} \tag{2.1.7}$$

The rewriting of the volume integral into a surface integral in the last step is analogous to Eq. 2.1.4. The moment must be an integral over the surface only, because the total force acts only on the surface. We can thus conclude that the stress tensor, just like the strain tensor, must be symmetric: $\sigma_{ij} = \sigma_{ji}$, such that the volume integral vanishes [3].

Let us now look at the thermodynamics of a deformation. If a small change in deformation occurs, the work done by the internal stresses δR can be determined by integrating $F_i \delta u_i$ over the volume (with δu_i the change in the displacement vector). We apply integration by parts for higher dimensions and use Gauss' divergence theorem (Eq. 2.1.4):

$$\begin{aligned} \int \delta R \mathrm{d}V &\equiv \int \frac{\partial \sigma_{ij}}{\partial x_j} \delta u_i \mathrm{d}V, \\ &= \int \left(\frac{\partial (\sigma_{ij} \delta u_i)}{\partial x_j} - \sigma_{ij} \frac{\partial \delta u_i}{\partial x_j} \right) \mathrm{d}V, \\ &= \oint \sigma_{ij} \delta u_i \mathrm{d}s_j - \int \sigma_{ij} \frac{\partial \delta u_i}{\partial x_j} \mathrm{d}V. \end{aligned}$$

To eliminate any small-sized system effects, we assume the deformed body to be of infinite size, and to be undeformed at infinity. The surface is then infinite as well, such that $\sigma_{ij} = 0$ on the surface. This reduces the surface integral to 0. Moreover, as a result of the symmetry of the stress tensor, we can rewrite $\int \delta R \mathrm{d}V$ as:

$$\begin{aligned} \int \delta R \mathrm{d}V &= -\int \sigma_{ij} \frac{\partial \delta u_i}{\partial x_j} \mathrm{d}V, \\ &= -\frac{1}{2} \int \sigma_{ij} \left(\frac{\partial \delta u_i}{\partial x_j} + \frac{\partial \delta u_j}{\partial x_i} \right) \mathrm{d}V, \\ &= -\int \sigma_{ij} \delta \epsilon_{ij} \mathrm{d}V. \end{aligned} \tag{2.1.8}$$

In the last step, we substituted an approximated form of the strain tensor (see Eq. 2.1.2), such that the product term of the strain tensor is neglected. The limitations of this approximation are discussed in Appendix A.

Assuming that the deformation occurs slowly enough to make the process thermodynamically reversible, the infinitesimal change in the free energy is equal to the difference between the heat acquired and the work done:

$$\mathrm{d}U = -S\mathrm{d}T + V\sigma_{ij}\mathrm{d}\epsilon_{ij},$$

such that

$$\sigma_{ij} = \frac{1}{V}\frac{\partial U}{\partial \epsilon_{ij}}.$$

In hydrostatic compression, i.e. when $\sigma_{ij} = -p\delta_{ij}$, the free energy reduces to its more familiar form: $\mathrm{d}U = -S\mathrm{d}T - p\mathrm{d}V$.

Let us now derive an expression for the free energy U as a function of the strain tensor for an isotropic body. We can simply expand U in terms of the strain tensor, because we assumed a small deformation. At zero strain, the internal stresses are equal to zero as well. It follows that there is no linear term in the expansion, as $0 = \sigma_{ij} = \partial U/\partial\epsilon_{ij}$. Furthermore, the free energy is a scalar. Therefore, every term in the expansion of U must be a scalar as well. The sums of the squares of the strain tensor are scalars. All together, this leads to the following expansion of the free energy [3]:

$$\frac{U}{V} = \frac{U_0}{V} + \frac{1}{2}\lambda\epsilon_{ii}^2 + \mu\epsilon_{ij}^2 + \mathcal{O}(\epsilon^3), \tag{2.1.9}$$

where λ and μ are called the Lamé coefficients. Note that no independent cross terms appear because the body is isotropic. That means that it does not matter what direction the deformation is in, only the nature of the deformation is important. The term ϵ_{ii}^2 represents the compression/expansion component, and ϵ_{ij}^2 represents the alteration of the shape. For a crystal, the situation is more complicated. A crystal is not isotropic, but ordered in a certain way. Therefore, it does matter what direction the deformation is in, because of its symmetries and planes. Take the face centred cubic (fcc) lattice for example: other internal stresses will occur for a deformation along the 100 plane as along the 111 plane, see Fig. 2.1.2. Therefore the free energy takes a more complicated form for a deformed crystal [3]:

$$\frac{U}{V} = \frac{1}{2}C_{ijkl}\epsilon_{ij}\epsilon_{kl}. \tag{2.1.10}$$

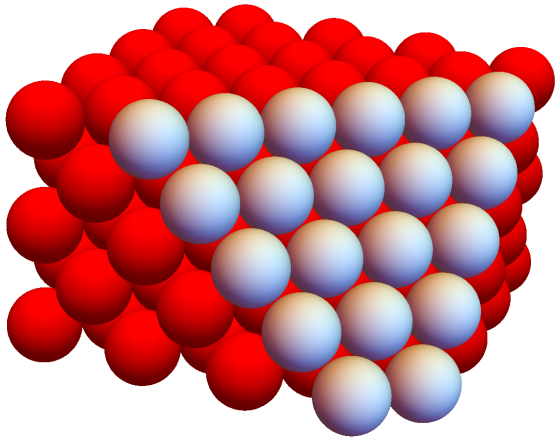

Figure 2.1.2: An fcc crystal showing different planes. The plane shown by the diagonal cross-section (blue) is the 111 plane, and the top plane is the 100 plane. As the arrangement of the particles is different in the different planes, a force along the 111 plane will result in a different stress as a force along the 100 plane.

We call C the "elastic modulus tensor," which is a tensor of rank four. Its coefficients are called the elastic constants. The indices are interchangeable because ϵ is symmetric. This means that in general, the number of independent coefficients of the tensor is 21. The stress tensor is now given by:

$$\sigma_{ij} = \frac{1}{V}\frac{\partial U}{\partial \epsilon_{ij}} = C_{ijkl}\epsilon_{kl}, \tag{2.1.11}$$

where

$$C_{ijkl} = \frac{1}{V}\frac{\partial^2 U}{\partial \epsilon_{ij}\partial \epsilon_{kl}}. \tag{2.1.12}$$

2.1.3 C_{11}, C_{12} and C_{44}

Apart from the symmetry in indices, other relations between the elastic modules coefficients can be found if the crystal possesses certain symmetries. This thesis' focus is on cubic crystals: the fcc for hard spheres, and the simple cubic crystal (sc) for hard cubes. The cubic crystal is a specific case of the tetragonal system, which is in the symmetry class C_{4v}. Taking the axis C_4 as the z-axis, and the xz-plane and yz-plane as the planes of symmetry, the following transformations are obtained by reflection through those planes:

xz-plane: $x \to x,\ y \to -y,\ z \to z$

and

yz-plane: $x \to -x,\ y \to y,\ z \to z.$

Therefore, all coefficients of the elastic modulus tensor that have an odd number of any one of the indices must vanish in order to uphold these transformations. This means that the general form of C_{ijkl} reduces to the following matrix:

$$C = \begin{pmatrix} C_{11} & C_{12} & C_{13} & 0 & 0 & 0 \\ C_{12} & C_{22} & C_{23} & 0 & 0 & 0 \\ C_{13} & C_{23} & C_{33} & 0 & 0 & 0 \\ 0 & 0 & 0 & C_{44} & 0 & 0 \\ 0 & 0 & 0 & 0 & C_{55} & 0 \\ 0 & 0 & 0 & 0 & 0 & C_{66} \end{pmatrix},$$

where the Voigt notation $C_{ijkl} = C_{ab}$ was applied, such that a and b take values from 1 to 6, in correspondence with the indices 11, 22, 33, 23, 13, 12 [20]. This notation will be applied whenever convenient from now on. Furthermore, the C_{4v} class exhibits rotational symmetry for a rotation through an angle of $\frac{1}{2}\pi$ around the z-axis. This provides the following transformations:

$x \to y,\ y \to -x,\ z \to z,$

which reduce the elastic modulus tensor even further:

$$C = \begin{pmatrix} C_{11} & C_{12} & C_{23} & 0 & 0 & 0 \\ C_{12} & C_{11} & C_{23} & 0 & 0 & 0 \\ C_{23} & C_{23} & C_{33} & 0 & 0 & 0 \\ 0 & 0 & 0 & C_{44} & 0 & 0 \\ 0 & 0 & 0 & 0 & C_{44} & 0 \\ 0 & 0 & 0 & 0 & 0 & C_{66} \end{pmatrix},$$

The general tetragonal system has no more symmetries to offer, but for the cubic system there is also symmetry through the rotations of $\frac{1}{2}\pi$ around the x- and y-axis, which brings about the last two transformations:

x-axis: $x \to x,\ y \to -z,\ z \to y,$

and

y-axis: $x \to z,\ y \to y,\ z \to -x.$

This results in the following elastic modulus tensor:

$$C = \begin{pmatrix} C_{11} & C_{12} & C_{12} & 0 & 0 & 0 \\ C_{12} & C_{11} & C_{12} & 0 & 0 & 0 \\ C_{12} & C_{12} & C_{11} & 0 & 0 & 0 \\ 0 & 0 & 0 & C_{44} & 0 & 0 \\ 0 & 0 & 0 & 0 & C_{44} & 0 \\ 0 & 0 & 0 & 0 & 0 & C_{44} \end{pmatrix}, \tag{2.1.13}$$

such that C_{11}, C_{12}, and C_{44} are the only three independent variables. From Eq. 2.1.12 ($\sigma_{ij} = C_{ijkl}\epsilon_{kl}$), we obtain the following relation between C_{11} and C_{12}:

$$C_{11} - C_{12} = \frac{1}{3}\sum_{i\neq j}^{3}\frac{\sigma_{ii} - \sigma_{jj}}{\epsilon_{ii} - \epsilon_{jj}}, \tag{2.1.14}$$

where we have used:

$$\begin{aligned}
\sigma_{ii} &= C_{iikl}\epsilon_{kl}, \\
&= C_{ii11}\epsilon_{11} + C_{ii22}\epsilon_{22} + C_{ii33}\epsilon_{33}, \\
\sigma_{11} &= C_{11}\epsilon_{11} + C_{12}(\epsilon_{22} + \epsilon_{33}), \\
\sigma_{22} &= C_{11}\epsilon_{22} + C_{12}(\epsilon_{11} + \epsilon_{33}), \\
\sigma_{33} &= C_{11}\epsilon_{33} + C_{12}(\epsilon_{11} + \epsilon_{22}).
\end{aligned} \tag{2.1.15}$$

We thus need another relation between C_{11} and C_{12} to be able to calculate them separately. In the following section, we derive the second relation. For C_{44} we end up with the following:

$$C_{44} = \frac{1}{3}\sum_{i\neq j}^{3}\frac{\sigma_{ij}}{2\epsilon_{ij}}, \tag{2.1.16}$$

where we have used:

$$\begin{aligned}
\sigma_{ij} &= C_{ij12}\epsilon_{12} + C_{ij21}\epsilon_{21} + C_{ij13}\epsilon_{13} + C_{ij31}\epsilon_{31} + C_{ij23}\epsilon_{23} + C_{ij32}\epsilon_{32}, \\
&= 2(C_{ij12}\epsilon_{12} + C_{ij13}\epsilon_{13} + C_{ij23}\epsilon_{23}), \\
\sigma_{12} &= 2C_{44}\epsilon_{12}, \\
\sigma_{13} &= 2C_{44}\epsilon_{13}, \\
\sigma_{23} &= 2C_{44}\epsilon_{23}.
\end{aligned}$$

All three components represent different deformations and reactions to those deformations. C_{11} and C_{12} both represent the effects of compression, with C_{11} expressing the change in length of the crystal in the direction parallel to the applied force, i.e. longitudinal compression, and C_{12} signifying the change in length in the directions perpendicular to the applied force, which is transverse expansion. C_{44} is a measure for the deformation as a result of a shear force. It represents the change in angle between the plane perpendicular to the applied force and the plane along which the force is applied. Figure 2.1.3 illustrates all effects in three diagrams. If some body exhibits larger elastic constants than another, it means that a larger force must be exerted on the body to reach the same deformation in comparison to the body with lower elastic constants.

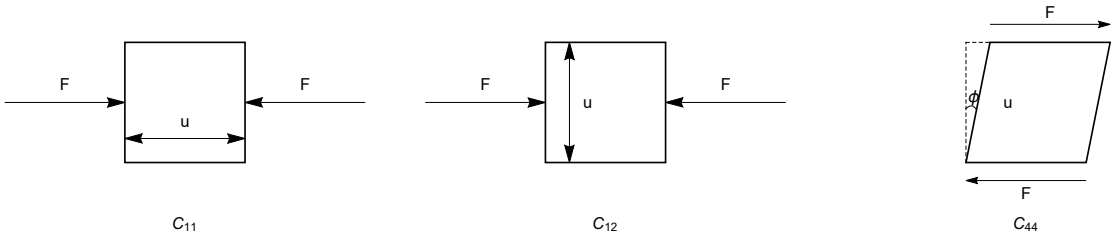

Figure 2.1.3: Diagrams exhibiting the different effects to different forces that the elastic constants represent. The left figure shows the internal force parallel to a compressing force, represented by the elastic constant C_{11}. The middle figure displays the internal force perpendicular to the compressing force, represented by C_{12}. The right figure shows the change in slant angle of the volume as a result of a shear force. This effect is represented by C_{44}.

2.1.4 Bulk Modulus B_0

We will now introduce the bulk modulus, which is a measure of the compressibility of a substance and is defined as $B_0 = -V\frac{\mathrm{d}p}{\mathrm{d}V}$. We will need the bulk modulus for the calculation of the elastic constants, as will be explained in Section 2.2.1. For isotropic bodies, B_0 can be expressed as a function of the Lamé constants: $B_0 = \lambda + \frac{2}{3}\mu$

[3]. For reasons that will become clear later, we want to find a similar expression for the bulk modulus of a crystal in terms of the elastic constants. To this end, we deform the system by applying a pure expansion matrix: $\mathbf{D} = \mathbf{I}(V/V_0)^{1/3}$. Then ϵ can be calculated as $\epsilon = \frac{1}{2}\left(\mathbf{D}^T\mathbf{D} - \mathbf{I}\right)$. First, we expand the free energy as a function of the strain ϵ_i:

$$\begin{aligned} U &= U(\epsilon = 0) + \frac{\mathrm{d}U}{\mathrm{d}\epsilon_i}\epsilon_i + \frac{1}{2}\frac{\mathrm{d}^2U}{\mathrm{d}\epsilon_i \mathrm{d}\epsilon_j}\epsilon_i\epsilon_j, \\ &= U(\epsilon = 0) + V_0\sigma_i\epsilon_i + \frac{V_0}{2}C_{ij}\epsilon_i\epsilon_j, \\ &= U(\epsilon = 0) + 3V_0 p\epsilon_1 + \frac{3}{2}V_0(C_{11} + 2C_{12})\epsilon_1^2, \end{aligned}$$

where $\sigma = p\mathbf{I}$ was used, which is true for hydrostatic expansion. Furthermore, $\epsilon_{i\leq 3} = \epsilon_1$, and $\epsilon_{i\geq 4} = 0$, because of the nature of the deformation. We expand the deformation matrix in the small volume change $\delta V = V - V_0$:

$$D_{ii} = \left(\frac{V}{V_0}\right)^{1/3} = \left(\frac{V_0 + \delta V}{V_0}\right)^{1/3} = \left(1 + \frac{\delta V}{V_0}\right)^{1/3} \approx 1 + \frac{1}{3}\frac{\delta V}{V_0}.$$

We now calculate the strain ϵ_1 and substitute it in the expression for the free energy:

$$\begin{aligned} \epsilon_1 &= \frac{1}{2}\left(D_{11}^2 - 1\right) = \frac{1}{2}\left(\frac{2}{3}\frac{\delta V}{V_0} + \frac{1}{9}\left(\frac{\delta V}{V_0}\right)^2\right), \\ U &= U(\epsilon = 0) + 3V_0 p\frac{1}{2}\left(\frac{2}{3}\frac{\delta V}{V_0} + \frac{1}{9}\left(\frac{\delta V}{V_0}\right)^2\right) + \frac{3}{2}V_0(C_{11} + 2C_{12})\left(\frac{1}{2}\left(\frac{2}{3}\frac{\delta V}{V_0} + \frac{1}{9}\left(\frac{\delta V}{V_0}\right)^2\right)\right)^2, \\ &= U(\epsilon = 0) + p\delta V + \frac{1}{2}\frac{C_{11} + 2C_{12} + p}{3V_0}\delta V^2 + \mathcal{O}(\delta V^3). \end{aligned}$$

The bulk modulus B_0 can now be expressed as a function of the two compression constants:

$$B_0 = -V\frac{\mathrm{d}p}{\mathrm{d}V} = V\frac{\mathrm{d}^2U}{\mathrm{d}V^2} = \frac{C_{11} + 2C_{12} + p}{3}, \tag{2.1.17}$$

providing the second relation between C_{11} and C_{12}. Together with Eqs. 2.1.14, and 2.1.16, the elastic constants can be calculated. In the following section, we discuss two methods of calculation.

2.2 Finding the Elastic Constants

We have now discussed all the necessary ingredients for the calculation of the elastic constants. Some methods do not calculate these constants directly however, but rather the so-called "effective elastic constants," defined as

$$B_{ijkl} = C_{ijkl} - p(\delta_{ik}\delta_{jl} + \delta_{il}\delta_{jk} - \delta_{ij}\delta_{kl}), \tag{2.2.1}$$

or in matrix form:

$$B = C - p\begin{pmatrix} 1 & -1 & -1 & 0 & 0 & 0 \\ -1 & 1 & -1 & 0 & 0 & 0 \\ -1 & -1 & 1 & 0 & 0 & 0 \\ 0 & 0 & 0 & 1 & 0 & 0 \\ 0 & 0 & 0 & 0 & 1 & 0 \\ 0 & 0 & 0 & 0 & 0 & 1 \end{pmatrix}. \tag{2.2.2}$$

The pressure term comes from the fact that even undeformed bodies experience hydrostatic compression under pressure. The methods that measure effective elastic constants do not account for this fact directly. Therefore, the pressure has to be added to or subtracted from the effective constants that were found. The relevant elastic constants can be related to the effective ones by:

$$C_{11} = B_{11} + p, \tag{2.2.3}$$
$$C_{12} = B_{12} - p, \tag{2.2.4}$$
$$C_{44} = B_{44} + p, \tag{2.2.5}$$

using the Voigt notation. The bulk modulus B_0 in terms of the effective constants becomes:

$$B_0 = -V\frac{\mathrm{d}p}{\mathrm{d}V} = \frac{B_{11}+2B_{12}}{3}. \tag{2.2.6}$$

In this thesis, we explore two methods of calculating the elastic constants of a cubic crystal. Both methods calculate the effective elastic constants. We will now discuss the two methods of calculation.

2.2.1 Method 1: Global Strain Fluctuations

As stated earlier, the elastic constants are a measure for the change in the shape of a body with respect to its equilibrium shape due to external forces. Every body is subject to fluctuations from its equilibrium shape, which cause internal stresses, just as external forces do. The higher the elastic constants of a specific body, the smaller these fluctuations will be. Therefore, the average fluctuation is a measure for the size of the elastic constants. Define the deformation matrix $\mathbf{h}$, and the equilibrium matrix $\langle\mathbf{h}\rangle$. Following Gusev et al. [21], we can use the Parrinello-Rahman fluctuation formula [21, 22]:

$$B_{ijkl} = \frac{k_B T}{\langle V\rangle}\langle\epsilon_{ij}\epsilon_{kl}\rangle^{-1}, \tag{2.2.7}$$

$$\epsilon = \frac{1}{2}\left(\langle\mathbf{h}\rangle^{-1,T}\mathbf{h}^T\mathbf{h}\langle\mathbf{h}\rangle^{-1}-\mathbf{I}\right), \tag{2.2.8}$$

$$\epsilon_{ij} = \frac{1}{2}\left(h_{nl}\langle h\rangle^{-1}_{lj}h_{np}\langle h\rangle^{-1}_{pi}-\delta_{ij}\right), \tag{2.2.9}$$

where B_{ijkl} are the effective elastic constants. These formulas can be applied to any crystal. However, the method is computationally very expensive, because it requires a lot of data to calculate averages accurately, let alone the average fluctuation around an average. Therefore, the elastic constants found by this method take a very long time to converge. In Section 3.1.5, we will explain in detail how we can measure $\langle\mathbf{h}\rangle$ and thus ϵ using Monte Carlo simulations.

2.2.2 Method 2: Stress-Strain Relation

The second method we employ makes use of the relation between the stress and strain via the elastic constants which was derived earlier in Eq. 2.1.11. Rewriting this relation in terms of the effective elastic constants B_{ijkl} and the effective stress tensor $\tilde{\sigma}$ gives:

$$\tilde{\sigma}_{ij} = B_{ijkl}\epsilon_{kl}. \tag{2.2.10}$$

Furthermore we use the relation between the deformation matrix and the strain tensor, derived in Eq. 2.1.3:

$$\epsilon = \frac{1}{2}(\mathbf{D}^T\mathbf{D}-\mathbf{I}).$$

When the system is placed under a constant deformation, the strain ϵ can be obtained. With Event Driven Molecular Dynamics (EDMD), the effective stress tensor can be extracted from the colliding particles in the system. With the known strain and the measured stress, the effective elastic constants can be calculated. We will discuss the implementation further in Section 3.2.

2.3 Simulation Methods

Different simulation techniques have been used to implement the two methods described in the previous section. We implemented the first method in Monte Carlo simulations, and the second in Event Driven Molecular Dynamics (EDMD). In the following two sections, the theoretical framework on which the techniques are based on will be explored.

2.3.1 Monte Carlo

The first simulation technique we discuss is the Monte Carlo method. We will use the Monte Carlo technique to implement the calculation method discussed in Section 2.2.1. Monte Carlo is a numerical method which is used for studying statistical problems in physics. Statistical physics is concerned with systems that consist of many components, typically many particles. A few of these systems can be solved exactly, such as the ideal gas.

However, in general the vast number of equations of motion makes it impossible to solve the system exactly. Nonetheless, looking at the macroscopic behaviour of the system, we find that the system follows a well-defined behaviour. The large number of equations of motion of the particles must average out to this macroscopic behaviour. One of the fundamental goals in statistical physics is the calculation of this average behaviour. That is why Monte Carlo is a viable simulation technique for the implementation of the first method of calculation, as this method calculates the elastic constants by the measurement of averages.

Suppose our system is in state A. Define $P(A \to B)\mathrm{d}t$ as the probability that the system evolves to state B in time $\mathrm{d}t$. $P(A \to B)$ is called the transition rate from A to B. There are many states B that state A can transit to. We treat this problem in a probabilistic way by assigning a set of weights $w_A(t)$ to the probability that the system is in state A at time t. Using the transition rate, we can calculate the change in this weight as [23]:

$$\frac{\mathrm{d}w_A}{\mathrm{d}t} = \sum_B [w_B(t)P(B \to A) - w_A(t)P(A \to B)]. \tag{2.3.1}$$

In a state of equilibrium, the two terms on the right hand side cancel each other, and the weights take constant values $p_A = \lim_{t\to\infty} w_A(t)$. In 1902, Gibbs showed that these equilibrium weights are equal to the Boltzmann distribution [23]:

$$p_A = \frac{1}{Z}\mathrm{e}^{-\beta E_A}, \tag{2.3.2}$$

where E_A is the energy of state A, and $\beta = 1/(k_B T)$ is the Boltzmann factor. Z is called the partition function and is the normalizing factor:

$$Z = \sum_A \mathrm{e}^{-\beta E_A}.$$

The goal of a Monte Carlo simulation is to generate states according to their proper weight, i.e. the Boltzmann distribution. If we can do this then we can calculate average quantities in our system using:

$$\langle A \rangle = \frac{1}{M}\sum_{i=1}^{M} A_i \left[\frac{\mathrm{e}^{-\beta E_{A_i}}}{Z}\right].$$

The trick will be to be able to go from a state A to B according to the correct transition rate $P(A \to B)$.

Choosing the right transition rate is not a trivial task. To make it possible, we make use of "Markov processes." The Markov process is a mechanism that transits the system from state A into a random other state B. The transition probability $P(A \to B)$ gives the probability that state B is generated from state A. It should satisfy two conditions: it should be constant over time, and it should only depend on state A and B, not on any other state. These two conditions make sure that the probability to end up in state B from state A remains constant. We have now described one Markov process. The Monte Carlo simulations then starts another Markov process, and another after that. We end up with a Markov chain of states, such that $A \to B \to C \to D \to \ldots$. In order to achieve the Boltzmann distribution in equilibrium we need two more conditions for the Markov chain: "ergodicity" and "detailed balance."

Ergodicity: The Markov process is defined in such a way that for every state A and Z, there exists a Markov chain $A \to B \to C \to \ldots \to Z$ such that the probability $P(A \to B \to C \to \ldots \to Z)$ is non-zero. That means that given enough time (i.e. enough Markov processes), the system can end up in any state Z. $Z = A$ is then possible as well: the system can remain in the same state. This ensures that eventually, the system will reach the equilibrium state. It does not matter what state the simulation was initiated in. This condition is called "ergodicity."

Detailed Balance: We will now derive the mathematical condition of detailed balance. This condition makes sure that we end up in the Boltzmann distribution in equilibrium. Using Eq. 2.3.1, we find that in equilibrium:

$$\sum_B p_A P(A \to B) = \sum_B p_B P(B \to A),$$

where we used that $\frac{\mathrm{d}w_A(t)}{\mathrm{d}t} = 0$ and $w_A(t) = p_A$ in equilibrium. Using the fact that $\sum_B P(A \to B) = 1$, this simplifies to the condition [23]:

$$p_A = \sum_B p_B P(B \to A).$$

However, not every transition probability that satisfies this condition also tends to the equilibrium distribution p_A. For that to happen we need the condition of detailed balance [23]:

$$p_A P(A \to B) = p_B P(B \to A), \tag{2.3.3}$$

such that the transition probabilities must satisfy:

$$\frac{P(A \to B)}{P(B \to A)} = \frac{p_B}{p_A} = \mathrm{e}^{-\beta(E_B - E_A)}, \tag{2.3.4}$$

to ensure that the probability distribution is equal to the Boltzmann distribution of Eq. 2.3.2. In Section 3.1 we explain how we implement this probability distribution in Monte Carlo simulations.

The evolution of the system and movement of particles in a Monte Carlo simulation are artificial, because any change in the system is tried at random and accepted by the certain probability we discussed. Therefore, only the average state of the system and the average positions of the particles are meaningful and only (semi-)equilibrium properties can be calculated with the Monte Carlo system. That is why we implement method 1, which is based on averages as explained in Sec. 2.2.1, in the Monte Carlo simulations. We use a different simulation technique for method 2 (Sec. 2.2.2): Event Driven Molecular Dynamics.

2.3.2 Event Driven Molecular Dynamics (EDMD)

In contrast to the Monte Carlo simulation, which has its foundation in equilibrium statistical physics, the Molecular Dynamics (MD) simulation method is based on Newton's equations of motion:

$$F = m\ddot{\vec{r}}, \tag{2.3.5}$$

$$\vec{p} = m\dot{\vec{r}}. \tag{2.3.6}$$

In a system with a large number of particles, the number of equations that has to be solved becomes large as well. Such a system cannot be solved exactly. Tracking the influence of neighbouring particles on each other provide the means to calculate the force on any given particle at any given time. The particle that is subject to that force then follows a trajectory that changes direction as the force exerted on the particle changes. Considering the force to be constant for a short period of time, this trajectory can be measured with fewer calculations. However, the longer the force is considered to be constant, the lower the accuracy of the measurement [24].

For hard particles, this accuracy problem vanishes, as the only time two hard particles influence each other, is when they collide. Between collisions the force is actually constant, so it is not an approximation as it would be for a different potential. This is what the Event Driven Molecular Dynamics (EDMD) simulation for hard particles is based on. The system evolves from collision to collision, updating the particles' positions along their trajectories. The particles are given an initial position and velocity, and the first upcoming collision (or event) is calculated. Specifically, consider two spheres i and j with a diameter of σ_s. Let $\vec{r_i}$ and $\vec{r_j}$ denote their positions at time t, and $\vec{v_i}$ and $\vec{v_j}$ the respective velocities. The two spheres collide at time $t + t_{ij}$, at which point the following equation is satisfied [25]:

$$v_{ij}^2 t_{ij}^2 = 2b_{ij}t_{ij} + r_{ij}^2 - \sigma_s^2 = 0, \tag{2.3.7}$$

with $b_{ij} = \vec{r_{ij}} \cdot \vec{v_{ij}}$, $\vec{r_{ij}} = \vec{r_i} - \vec{r_j}$, and $\vec{v_{ij}} = \vec{v_i} - \vec{v_j}$. The first upcoming collision can be found efficiently using a binary tree [26]. The pressure can be extracted from the chain of collisions in time period Δt using the collisional virial [25]:

$$\frac{\beta PV}{N} = 1 + \frac{\beta}{3\Delta t N} \sum_{\text{colls}} \vec{r_{ij}} \cdot \delta\vec{p_i}. \tag{2.3.8}$$

The possibility to calculate the pressure is an essential characteristic of the EDMD method. In the Monte Carlo simulations, this is impossible for hard particles: the pressure cannot get extracted from the hard potential,

and there is no information on collisions as they do not occur. This is not a problem for the first method of calculation of elastic constants, because the pressure is fixed and the system has an equilibrium volume. For the second method however, the volume needs to be fixed, and therefore the pressure must be calculated in order to be able to use Eqs. 2.2.3 - 2.2.5. Section 3.2 elaborates on the implementation of the calculation method.

Chapter 3

Methods

In this chapter we elaborate on the implementation of the two methods of calculating elastic constants that were discussed in Section 2.2.1 and 2.2.2. First we will discuss the mechanics of the Monte Carlo method after which we will explain how the elastic modulus tensor can be calculated using this simulation. Then we will elaborate on the calculation of the elastic constants using the EDMD simulation technique.

3.1 Simulation Method 1: Monte Carlo

The Monte Carlo simulation technique is based on statistics, as explained in Section 2.3.1. The simulations run the system through different states, where each transition is accepted or not with some probability. This probability is equal to the Boltzmann distribution in equilibrium. If the system runs long enough, it will end up in its equilibrium state. In principle, this does not depend on the initial configuration of the system. However, in practice huge free-energy barriers can separate the initial from the equilibrium state, making it essentially impossible for the system to transition to the more stable part of phase space. It is therefore wise to be well informed on the effects of the parameters of the system. The system can then be set up in a configuration that is close to equilibrium. In the next section, we will explain how we set up the initial configuration.

The other main ingredient of the Monte Carlo simulation is the way the system evolves from one configuration to the other. In our case, the necessary moves of the system are volume and particle moves. In Section 3.1.2, we will explain how the particles move around and how the volume changes throughout the simulation.

3.1.1 Initializing the System

The system we simulate is in an NPT-ensemble. That means that the number of particles, pressure and temperature are fixed. The volume is subject to change. The simulated volume forms a parallelepiped and is thus spanned by three vectors. Together, they form a matrix which we call the "boxvector matrix." Initially, this is a 3×3 diagonal matrix, where the non-zero elements are equal to the edge-length of the box. All particles are initially placed on their crystalline lattice. For the spheres the face centred cubic configuration is used, and for the cubes a simple cubic configuration. The distance between the particles depends on the initial packing fraction.

As has been explained earlier, the Monte Carlo simulated system needs time to reach its equilibrium state. During this time, measurements on the system are not useful, except for knowing whether the system has equilibrated yet. It is therefore good to choose a packing fraction that is close to the equilibrium value for the set number of particles, pressure and temperature. For hard spheres with a diameter of σ_s, we can use the Speedy equation of state in order to accomplish this [27]:

$$\frac{pV}{Nk_BT} = \frac{3}{1-z} - \frac{a(z-b)}{z-c}, \tag{3.1.1}$$

where:

$$z = \frac{N\sigma_s^3}{V\sqrt{2}}, \tag{3.1.2}$$

$$a = 0.5921, \tag{3.1.3}$$

$$b = 0.7072, \tag{3.1.4}$$

$$c = 0.601. \tag{3.1.5}$$

We can also use the Speedy equation of state to check whether our the simulation ends up in the right equilibrium volume. For hard cubes, an analytic model for the equation of state has not been formulated yet.

The procedure explained above simulates a finite volume, while we assumed an infinite volume in the derivation of the strain tensor (Section 2.1.1). To eliminate boundary effects in the simulated system, we induced periodic boundary conditions on the volume. This means that when a particle moves outside the simulated volume at one side, it comes into the box again at the other side. Therefore, particles on opposite sides of the simulation box can still be seen as close to each other. This is illustrated by Fig. 3.1.1. The centre box is the simulated volume. The green particles in the figure are all close to each other via the periodic boundary conditions.

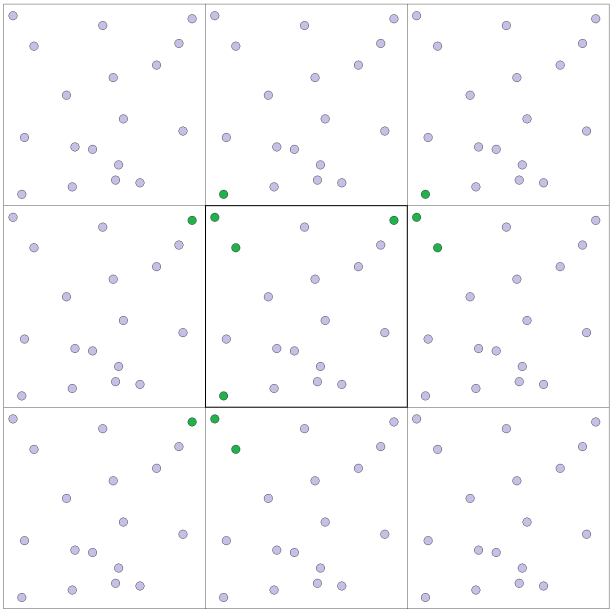

Figure 3.1.1: Infinite volume created by using periodic boundary conditions. The centre box is the simulated box; the surrounding boxes are periodic versions of the centre box. The green particles all interact with each other via the periodic boundary conditions.

This means that the distance between the centres of mass of two particles i and j with positions r_i and r_j is calculated as follows:

$$r_{ik} - r_{jk} = \begin{cases} r_{ik} - r_{jk} - \frac{r_{ik}-r_{jk}}{|r_{ik}-r_{jk}|} \cdot \text{box}_k & \text{if } |r_{ik} - r_{jk}| > \frac{1}{2}\text{box}_k, \\ r_{ik} - r_{jk} & \text{else,} \end{cases} \tag{3.1.6}$$

where r_{ik} and r_{jk} are elements of the vectors r_i and r_j respectively, and box_k is the length of the simulated volume in direction k. In words, this means that when two particles lie further than half a box away from each other, we subtract or add the box length.

3.1.2 Evolution of the System

After the initialization of the system, we can start to evolve it by means of Monte Carlo steps. In this section, we discuss the two moves needed to calculate the elastic constants: the particle move and the volume move. Right after initialization, only particle moves are allowed. This is to prevent the system from collapsing to a very high packing fraction immediately at high pressures. When the particles are somewhat scrambled, this

will not happen.

Like the moves themselves, which move will be undertaken next is random as well. Before making a move, an integer in the range [0,10) is picked at random. If this integer equals 0, we try a volume move, and otherwise we try a particle move. This randomization of the moves obeys detailed balance: the chance to try to do a particle or volume move is equal to the chance to try to undo that same move.

3.1.2.1 Particle Movement

The hard particle system evolves by means of Monte Carlo steps. One of the particles is picked at random, after which a random movement is imposed on that particle. The distance between its original position and its new one is set to be smaller than the particles' diameter for the spheres, or the length of the edges of the cubes for the cubic particles. The proposed move now gets accepted with the following probability:

$$P(A \to B) \quad = \quad \mathrm{e}^{-\beta \Delta U}, \tag{3.1.7}$$

where $\beta = k_B T$. We are only concerned with hard particles in this thesis. That means that the energy only changes when the proposed move causes two or more particles to overlap, in which case the energy becomes infinite. The acceptance rate for hard particles thus simplifies to:

$$P(A \to B) \quad = \quad \begin{cases} \mathrm{e}^{-\beta \cdot \infty} = 0 & \text{particles overlap,} \\ \mathrm{e}^{-\beta \cdot 0} = 1 & \text{particles do not overlap.} \end{cases} \tag{3.1.8}$$

We see that the trial particle move is always accepted if it does not cause any overlap, and always rejected when it does cause overlap. This principle is illustrated for spherical particles in Fig. 3.1.2. For cubes, there are two sorts of particle moves: the translational one and the rotational one. The principle of acceptance is the same for both moves. After the acceptance or rejection of the trial move, the next Markov process is initiated, as explained before.

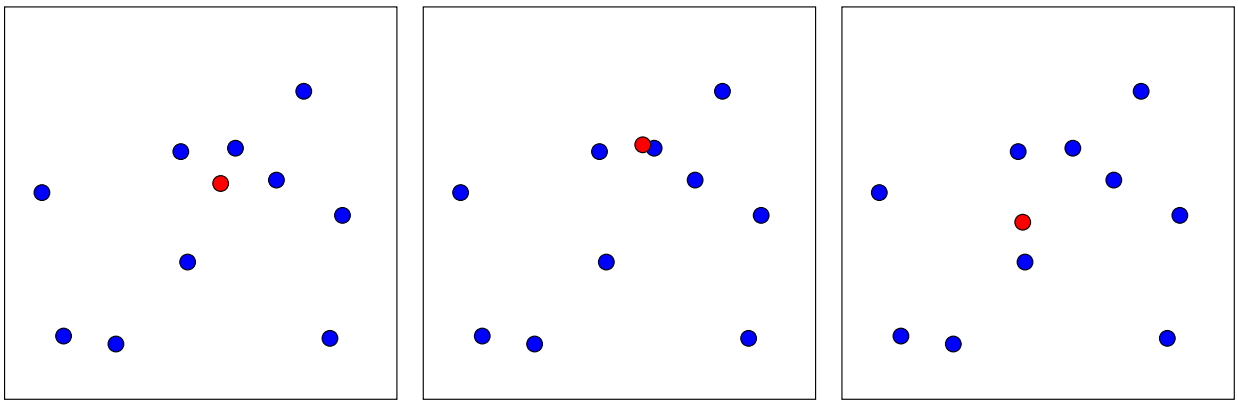

(a) Red particle is picked at random. A translational move is tried.

(b) Particle move causes the particle to overlap with another particle and is therefore rejected.

(c) Particle move causes no overlap and is therefore accepted.

Figure 3.1.2: Monte Carlo particle move acceptance/rejection schematics.

During the simulations relative particle positions have been used, by multiplying the particle vectors by the inverse of the boxmatrix. This can easily be undone by multiplying with the current boxvector, to get the actual particle positions. These relative positions ensure the possibility to use a much more pragmatic method to perform the overlap checks and the use of a cell list, which we explain in Section 3.1.4. For any snapshots made during the simulations, the true particle position will be used.

3.1.2.2 Volume Deformation

A much more involved move than the particle move is the volume move. In our system, not only the size but also the shape of the volume can change. During a volume trial move, one of the elements of the upper

triangular boxvector matrix is picked at random, and a small number $|\Delta V| < 0.5\delta V$ is added to that element. This method of changing the volume is called "floppy box." The determination of δV is explained later on. There are two cases in which the volume move is rejected: either the box has become so flat that the particles do not fit anymore, or it gets rejected on basis of the acceptance probability. We test for the two rejection cases in said order. The second case will be explained now.

As with the particle move, the volume move is accepted with a probability:

$$P(A \to B) \quad = \quad \exp\left[-\beta(U_B - U_A) - \beta p\left(V_B - V_A + N\ln(V_B/V_A)\right)\right].$$

However, for hard particles U_A was always zero. Moreover, the new energy of state B, U_B, will be equal to infinity if the volume move causes overlap, and equal to 0 if it does not. The acceptance probability therefore takes the form:

$$P(A \to B) \quad = \quad \begin{cases} \mathrm{e}^{-\beta p(V_B - V_A)}\left(\frac{V_B}{V_A}\right)^N & \text{particles do not overlap,} \\ 0 & \text{particles overlap.} \end{cases} \tag{3.1.9}$$

When we try a volume move, we pick a random number between 0 and 1. If this number is higher than the non-overlapping case of the acceptance rate $P(A \to B)$, the move is rejected. If it is lower or equal to the acceptance rate, we check for overlap between the particles. If any two particles overlap, the acceptance rate should be equal to 0. The volume move is thus rejected and the boxvector matrix restored. Both cases are illustrated in Fig. 3.1.3.

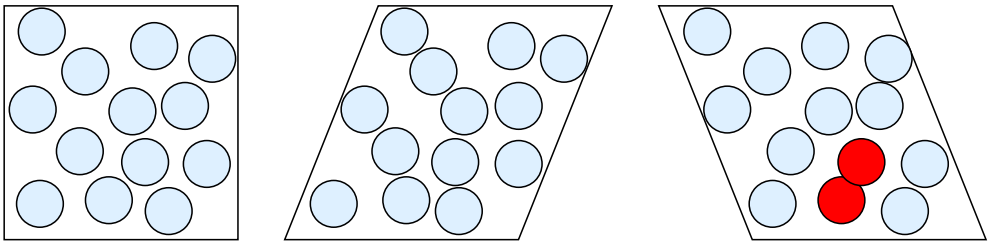

Figure 3.1.3: Two different shearing deformations of the original system on the left. The deformation in the middle is allowed as there is no overlap between any two particles. The deformation on the right is rejected, because the two red particles overlap as a result of the deformation.

The volume deformation is a very slow move to make, and becomes exponentially slower as the simulation is done with an increasing number of particles. For the particle move, only the moved particle could cause overlap. For the volume move, any two particles might overlap. The efficiency can be vastly improved by the use of a cell list, which decreases the number of particles to be checked for overlap. The implementation of the cell list will be explained in Section 3.1.4.

Choice of δV: We start with an initial value for δV equal to $\delta V = 0.1\sigma_{s,c}$, with σ_s the diameter for spheres and σ_c the side length for cubes. During the first 500,000 Monte Carlo cycles (N Monte Carlo steps are equal to 1 Monte Carlo cycle), we monitor the acceptance rate of the volume change. Eventually, this should be approximately 10%. This balances the size of the volume moves in such a way that they are accepted frequently enough and are still of sufficient size to have an effect. This way the system can equilibrate as fast as possible to the proper equation of state. After every 10,000 Monte Carlo cycles, the acceptance ratio of the tried volume deformation is calculated. If that rate turns out to be smaller than 8%, we divide δV with a factor of 1.7, and if the rate is larger than 15%, we multiply δV with a factor of 1.3. This way, after the first 500,000 Monte Carlo cycles, a δV is acquired that results in an acceptance ratio between 8% and 15%. The process of finding the right δV does not have a significant effect on the equilibration.

3.1.3 Checking for Overlap

We have seen that for both the particle and the volume move, the acceptance rate depends on whether any two particles overlap. In this section, we explain how the overlap check works for spheres and for cubes. Note that we use relative positions, such that the coordinates of the particles lie between 0 and 1.

3.1.3.1 Spheres

For spheres it is very straightforward to check whether two particles overlap. First we determine the vector $\vec{r}_{12}$ between the centres of the two particles. Note that the periodic boundary conditions should be taken into account: when two particles lie more than 0.5 (in relative coordinates) away from each other in one of the directions, 1 should be added or subtracted from the element in that direction. Then the vector is transformed to the real volume system. If the length of the vector is smaller than the sum of the two radii of the spheres, the two spheres overlap and the translational or deformation move has to be rejected. If the length is greater than that, the two particles do not overlap, and the next pair can be checked. For cubes there is more work to it, as we will explain now.

3.1.3.2 Cubes

The first step in checking whether two cubes overlap is the same as for spheres. The vector $\vec{r}_{12}$ between the two centres of mass is calculated, while taking the periodic boundary conditions into account, and transformed to the real volume system. If the vector length is greater than the interaction length d_{out}, the two cubes do not overlap, where d_{out} is the diameter of the circumscribed sphere. Note that this equals $\sigma_c\sqrt{3}$ for a cube, where σ_c is the edge-length . If the vector length is smaller than the diameter of the inscribed sphere of the cubes d_{in}, the particles definitely overlap. In any other case, the Separating Axis Theorem is used to determine whether they overlap or not.

3.1.3.3 Separating Axis Theorem (SAT)

The Separating Axis Theorem (SAT) states that two convex objects do not overlap if and only if there exists an axis on which the projections of the two objects do not overlap. If there exists no such axis, the two objects do overlap [28]. This is illustrated by Fig. 3.1.4. It can be shown that the only axes that need to be checked for overlap are the normals to all faces of both particles and all the possible cross products between the normals of one particle, and the normals of the other. If the projections overlap on all these axes, there is no need to search any further and it can be concluded that the two particles overlap.

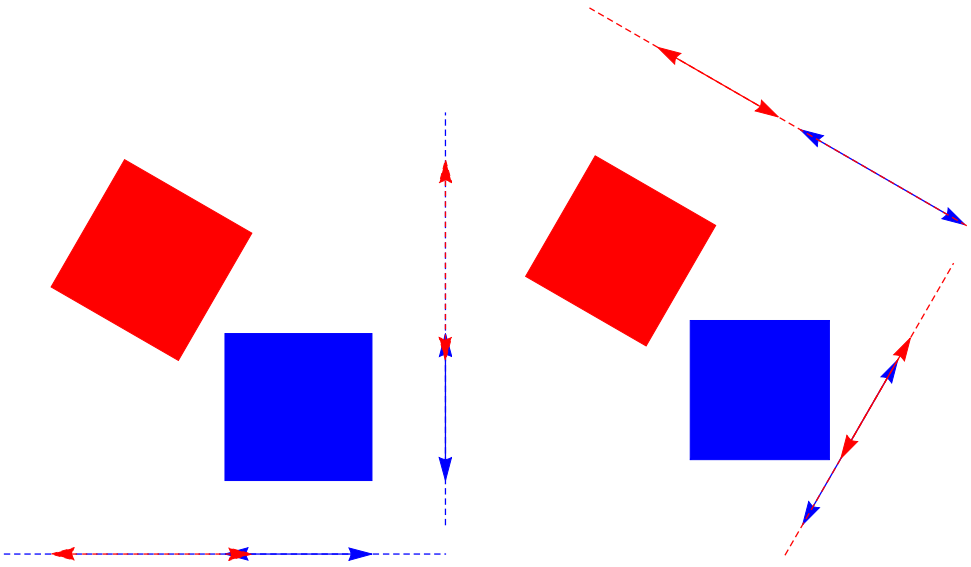

Figure 3.1.4: Illustration of how the projection of particles on the normals of these particles can be used to determine whether the particles overlap. In the left figure, the projections on the normals of the blue square overlap. In the right picture, the projections on the upper normal do not overlap. Thus, the two squares do not overlap.

If the inner product of the transformed vector $\vec{r}_{12}$ and the examined axis is smaller than d_{in}, the projections will overlap, and the actual projections do not need to be calculated. The process can now be repeated for the next axis. If this is not the case, the two projections are calculated, and their minimum and maximum are compared to check whether they overlap on the checked axis. If the projections do not overlap on any of the relevant axes, the two particles do not overlap and the next two particles can be reviewed. If we check all

particle pairs this way, the overlap check becomes a needlessly slow process. In the next section, we discuss a way to speed up the process by using a cell list.

3.1.4 Efficiency

To make the overlap check more efficient, we employ a cell list. The cell list divides the total volume into multiple cells, such that all cells together cover the entire volume. The shortest distance from one side to another of the cells is set to be larger than the interaction length of the particles. The size of the cells has an upper boundary as well to ensure maximized efficiency. When the cell size surpasses this boundary due to a volume move, the cell list is redrawn with smaller cells. Each particle is assigned to its corresponding cell. Due to the definition of the cells, particles can now only overlap with particles of which the centre of mass lies within a neighbouring or the same cell. This is illustrated by Fig. 3.1.5. Because the particle positions are

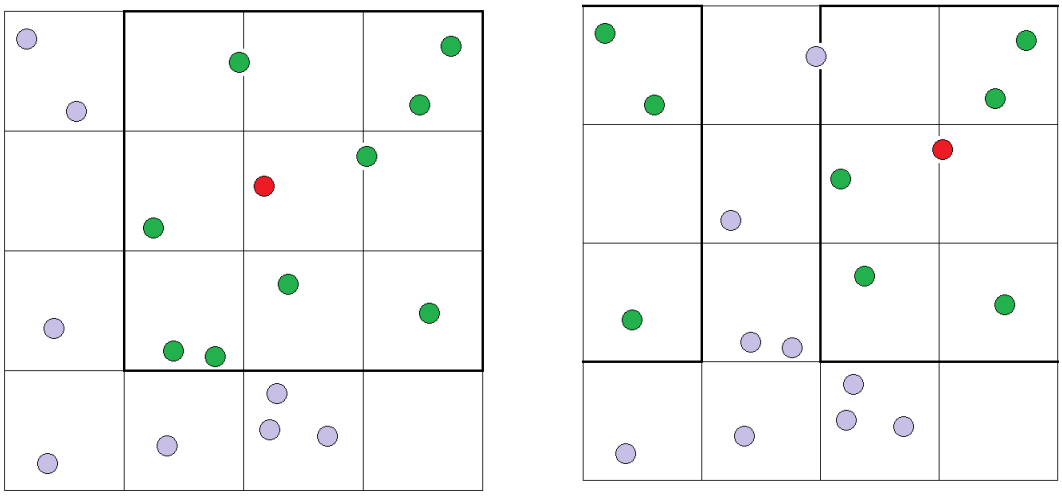

(a) The red particle can only interact with the green particles. Particles in non-neighbouring cells lie further than the interaction length away.

(b) Periodic boundary conditions are imposed on the cell list.

Figure 3.1.5: Functioning of the cell list

defined relative to a unit box volume, they do not change when the volume is deformed or resized. The cells are denoted by their place in all three directions. This means that cell (0, 3, 2) is on the first place in the x-direction, third in the y-direction and second in the z-direction. The cell corresponding to a particle is then in all three directions equal to the floor function of i^{th} element of the position vector of the particle multiplied by the number of cells in direction i: floor(pos[part, i] $\cdot$ cells[i]). This shows one of the advantages of the use of relative positions. The floor function could not have been used if the real positions would have been used, because the positions might be shifted with respect to a cubic volume.

Defining the cells and particle positions relative to the unit volume also makes sure that the cell list does not need to be redrawn for every volume deformation. When a deformation is applied to the real volume however, it should be tested that the deformation does not cause the cells to become too flat (such that the shortest distance in the cell is smaller than the interaction length), if the cells were to be transformed to the real volume. Otherwise, the overlap check might fail to find a certain overlap, as not every pair that is within interaction range will be checked. If the cells do become too flat, the cell list has to be redrawn.

3.1.5 Calculating the Elastic Modulus Tensor

In Section 2.2.1, it was shown how to calculate the effective elastic constants from the average fluctuations of the volume from the equilibrium state. The following formulas are needed:

$$B_{ijkl} = \frac{k_B T}{\langle V \rangle} \langle \epsilon_{ij} \epsilon_{kl} \rangle^{-1}, \tag{3.1.10}$$

$$\epsilon = \frac{1}{2} \left(\langle \mathbf{h} \rangle^{-1,T} \mathbf{h}^T \mathbf{h} \langle \mathbf{h} \rangle^{-1} - \mathbf{I} \right), \tag{3.1.11}$$

$$\epsilon_{ij} = \frac{1}{2} \left(h_{nl} \langle h \rangle^{-1}_{lj} h_{np} \langle h \rangle^{-1}_{pi} - \delta_{ij} \right), \tag{3.1.12}$$

where $\mathbf{h}$ is the measured and $\langle \mathbf{h} \rangle$ the reference boxvector matrix, δ_{ij} the Kronecker delta, and all double indices are summed over.

After every 10 Monte Carlo cycles, the boxvector matrix is written to a file. When the simulation is finished, the first quarter of the data is dropped from the data set to account for equilibration time. The reference matrix $\langle \mathbf{h} \rangle$ is taken to be a diagonal matrix. Its non-zero elements are equal to the one-third of the determinant of the average of all boxvector matrices, so equal to one-third of the average volume. Using this reference matrix, the strain matrix can be calculated. Equation 3.1.11, gives a 3×3 matrix. Calculating the product to find the elastic constants using Eq. 3.1.10 needs some thorough thought. When calculating the product of the strain matrix elements, a 3×3 matrix is obtained, of which every element is again a 3×3 matrix itself. We call this matrix the "Smatrix." The elastic modulus tensor should be a simple 6×6 matrix. Thus, we need to extract the right elements from the Smatrix.

The final product matrix $\langle \epsilon_{ij} \epsilon_{kl} \rangle$ is calculated with the help of the Voigt notation, which transforms (i, j) as: $(1,1) \rightarrow 1$, $(2,2) \rightarrow 2$, $(3,3) \rightarrow 3$, $(2,3) \rightarrow 4$, $(1,3) \rightarrow 5$, $(1,2) \rightarrow 6$. The $(a, b)^{\text{th}}$ element of the final product matrix is then equal to the $(i, j, k, l)^{\text{th}}$ element of the Smatrix. (i, j) is transformed to a and (k, l) to b using the Voigt notation. The elements for which a or b is greater than 3 are then multiplied by 2, and the elements for which both a and b are greater than 3 are multiplied by 4. This is necessary because the Voigt number 4, 5, and 6 represent both terms (x, y) and (y, x), with $x \neq y$, due to symmetry. Now that the final product matrix has been obtained, the elastic constant matrix can be found by taking its inverse and dividing by the average volume. We calculate the inverse indirectly to avoid mixing with terms that should be equal to 0. We define S_{11} as the average of the elements (11), (22), and (33) of the product matrix; S_{12} as the average of (12), (13), and (23); and S_{44} as the average of (44), (55), and (66). The effective elastic constants are then equal to:

$$B_{11} = \frac{1}{3} \left(\frac{1}{S_{11} + 2S_{12}} + \frac{2}{S_{11} - S_{12}} \right),$$

$$B_{12} = \frac{1}{3} \left(\frac{1}{S_{11} + 2S_{12}} - \frac{1}{S_{11} - S_{12}} \right),$$

$$B_{44} = \frac{1}{S_{44}}.$$

The real elastic constants can then be calculated using Eqs. 2.2.3 - 2.2.5:

$$C_{11} = B_{11} + p,$$

$$C_{12} = B_{12} - p,$$

$$C_{44} = B_{44} + p.$$

3.2 Simulation Method 2: Event Driven Molecular Dynamics (EDMD)

We use the EDMD method to simulate a system with fixed number of particles, volume, and temperature (NVT-system). The pressure can be calculated during the simulations, as discussed in Section 2.3.2. It is much faster than the MC method, which is why the EDMD method has been used to generate all data for the cubic particles. We used an EDMD code from Smallenburg [16]. The input variables are the packing fraction η, number of particles N, number of lattice sites, and the strain variables "shiftx," "shifty" and "stretchz." Hard

spheres are placed on a face centred cubic lattice; hard cubes are placed on a simple cubic lattice of equal size in all three directions. When the number of lattice sites is larger than the number of particles, vacancies will be created on random lattice sites. The strain variables deform the lattice as follows:

$$D(\text{shiftx} = \delta) = \begin{pmatrix} 1 & 0 & \delta \\ 0 & 1 & 0 \\ 0 & 0 & 1 \end{pmatrix}, \quad D(\text{shifty} = \delta) = \begin{pmatrix} 1 & 0 & 0 \\ 0 & 1 & \delta \\ 0 & 0 & 1 \end{pmatrix}, \tag{3.2.1}$$

$$D(\text{stretchz} = \delta) = \begin{pmatrix} 1+\delta & 0 & 0 \\ 0 & 1-\delta & 0 \\ 0 & 0 & \frac{1}{1-\delta^2} \end{pmatrix}, \tag{3.2.2}$$

assuming only one of the strain variables is non-zero. We consider a cubic volume, such that the initial boxvector matrix is equal to $\sqrt[3]{V}\mathbf{I}$. The initial sizes of the simulated volume (box_x, box_y, and box_z) change as follows when a stretch deformation is applied:

$$\begin{aligned} \text{box}_x &= \sqrt[3]{V} \cdot (1 + \text{stretchz}), \\ \text{box}_y &= \sqrt[3]{V} \cdot (1 - \text{stretchz}), \\ \text{box}_z &= \sqrt[3]{V}/(1 - \text{stretchz}^2). \end{aligned}$$

The positions of the particles shift when a shear deformation is applied:

$$\begin{aligned} \text{pos}[x] &= \text{pos}[x] - \text{shiftx} \cdot \frac{\text{pos}[z]}{\text{box}_z}, \\ \text{pos}[y] &= \text{pos}[y] - \text{shifty} \cdot \frac{\text{pos}[z]}{\text{box}_z}, \\ \text{pos}[z] &= \text{pos}[z]. \end{aligned}$$

For the sheared system, the periodic boundary conditions shift as well. The conditions in the x- and y-direction stay the same as in Eq. 3.1.6. When two particles i and j with respective positions r_i and r_j lie further than half a box away in the z-direction we have:

$$x_i - x_j = x_i - x_j + \frac{z_i - z_j}{|z_i - z_j|} \cdot \text{shiftx}, \tag{3.2.3}$$

$$y_i - y_j = y_i - y_j + \frac{z_i - z_j}{|z_i - z_j|} \cdot \text{shifty}, \tag{3.2.4}$$

$$z_i - z_j = z_i - z_j - \frac{z_i - z_j}{|z_i - z_j|} \cdot \text{box}_z. \tag{3.2.5}$$

The shifted boundary conditions are illustrated in Fig. 3.2.1. Now that we have established what happens for

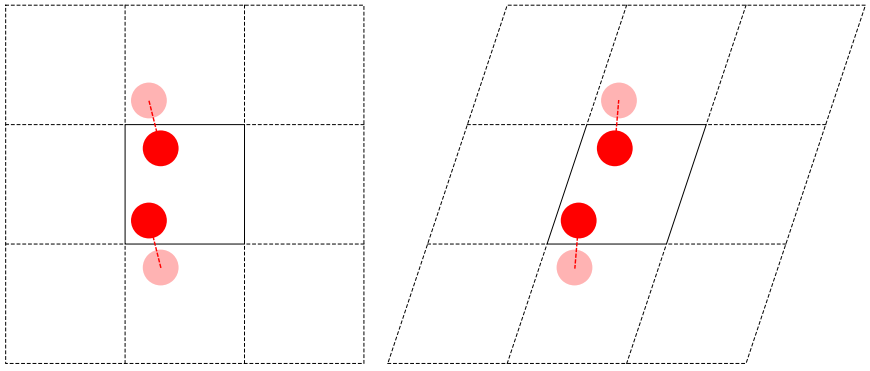

Figure 3.2.1: The difference in periodic boundary conditions for a regular system (left) and a shifted system (right). The pink particles are the periodic versions of the red particles. In the shifted system, the periodic boxes are shifted as well.

non-zero values of shiftx, shifty and stretchz, we can explain how this will help us calculate the elastic constants. First we discuss the calculation of C_{11} and C_{12}, then we move on to C_{44}.

3.2.1 Calculating C_{11} and C_{12}

A non-zero value of δ for stretchz results in the expansion of the volume in the x-direction, and compression in the y-direction or vice versa, corrected in the z-direction to keep the volume constant. This results in the following deformation matrix and stress tensor:

$$D(\delta) = \begin{pmatrix} 1+\delta & 0 & 0 \\ 0 & 1-\delta & 0 \\ 0 & 0 & \frac{1}{1-\delta^2} \end{pmatrix}, \qquad \epsilon = \begin{pmatrix} \frac{1}{2}((1+\delta)^2-1) & 0 & 0 \\ 0 & \frac{1}{2}((1-\delta)^2-1) & 0 \\ 0 & 0 & \frac{1}{2}\left(\frac{1}{(1-\delta^2)^2}-1\right) \end{pmatrix}. \quad (3.2.6)$$

Both the stress tensor and the equation of state can be measured by running the code. Using Eq. 2.2.10 and the expression for the bulk modulus B_0 (Eq. 2.2.6), the effective elastic constants B_{11} and B_{12} can be calculated as follows:

$$B_{11} - B_{12} = \frac{1}{3}\sum_{i\neq j}^{3} \frac{\tilde{\sigma}_i - \tilde{\sigma}_j}{\epsilon_i - \epsilon_j}, \quad (3.2.7)$$

$$\frac{1}{3}(B_{11} + 2B_{12}) = B_0 = -V\frac{\mathrm{d}p}{\mathrm{d}V}. \quad (3.2.8)$$

Solving these two linear equations results in the effective elastic constants B_{11} and B_{12}. Now the elastic constants can be determined using Eqs. 2.2.3 and 2.2.4:

$$C_{11} = B_{11} + p, \quad (3.2.9)$$

$$C_{12} = B_{12} - p. \quad (3.2.10)$$

For the hard sphere system, the Speedy equation of state (Eq. 3.1.1) was used to determine the bulk modulus B_0:

$$B_0 = -V\frac{\mathrm{d}}{\mathrm{d}V}\left[\frac{Nk_BT}{V}\left(\frac{3}{1-z} - \frac{a(z-b)}{z-c}\right)\right]. \quad (3.2.11)$$

3.2.2 Calculating C_{44}

A non-zero value of δ for shiftx results in a shift along the x-axis. Each particle is shifted proportionally to their position in the z-direction. This results in the following deformation matrix and strain tensor:

$$D(\delta) = \begin{pmatrix} 1 & 0 & \delta \\ 0 & 1 & 0 \\ 0 & 0 & 1 \end{pmatrix}, \qquad \epsilon = \begin{pmatrix} 0 & 0 & \frac{\delta}{2} \\ 0 & 0 & 0 \\ \frac{\delta}{2} & 0 & \frac{\delta^2}{2} \end{pmatrix}. \quad (3.2.12)$$

The elastic constant C_{44} is then given by:

$$C_{44} = \frac{\tilde{\sigma}_5}{2\epsilon_5} + p = \frac{\tilde{\sigma}_5}{\delta} + p. \quad (3.2.13)$$

We will calculate the elastic constants at different densities and, in the case of hard cubes, for different vacancy concentrations $v = \frac{\#vacancies}{\#lattice\ sites}$. In the next chapter, we discuss the results of the calculations of the elastic constants using both the MC and EDMD simulations. Subsequently, we will examine the correlation between the direction of the defects and the deformations applied to the crystal. In the next section, we explain how the direction of the defects can be found.

3.3 Tracking Vacancies

The vacancies can be tracked when the positions of all particles are known. We define a vacancy to be at a lattice site which is not the nearest lattice site of any particle. To use this definition, the positions of the lattice sites must be known. During an EDMD simulation however, the origin of the lattice can drift away from its original position [29]. We determine the size of this drift in all directions using the density profile of the particles in each direction, averaged over the other two directions. The density profile in the x-direction can be determined by counting the number of particles in the rectangular volume of $\mathrm{d}x \times \mathrm{box}_y \times \mathrm{box}_z$, such that the x-direction is divided in $\mathrm{box}_x/\mathrm{d}x$ number of parts. Thereby, we create a histogram of the number of particles

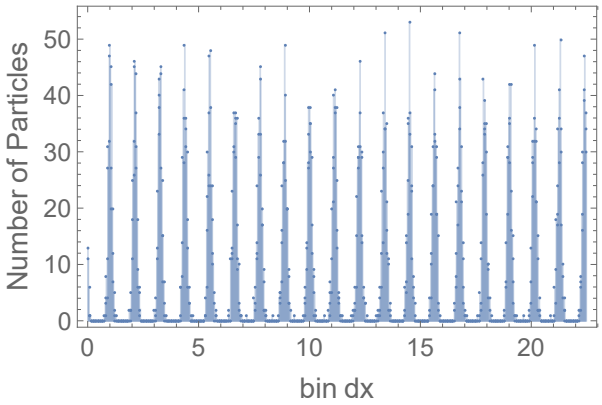

Figure 3.3.1: The number of particles counted in the region $\mathrm{d}x\{(\mathrm{bin}-1),\mathrm{bin}\}$.

in direction x averaged over the directions y and z (see Fig. 3.3.1). The same can be done for the directions y and z. For the sheared system, the density profile of the x-direction cannot be averaged over the z-direction directly, because the lattice sites are shifted with respect to each other. We correct for this fact by undoing the shift first, by placing a shift in the opposite direction on the particles. When the lattice is not deformed or distorted, the density profile shows distinct peaks with the highest concentration of particles. We can then fit a sinusoidal function: $f(x) = c(\sin[a(x-b)]+1)$ to the histogram, where a is the period, b the drift of the lattice and c the amplitude. We have thus found the drift b of the lattice. Using the shift, we place one of the lattice sites at the origin, and change the positions of the particles in the same way. Now we can find the empty lattice sites by calculating for each particle which lattice site is nearest to that particle. If a certain lattice does not belong to any particle, it must be a vacancy.

Let us take a look at the particles surrounding a vacancy. We define the direction of the defect as the direction in which the two particles surrounding the vacancy are closest to each other, see Fig. 3.3.2. In the stretched system, the distance between the lattice sites is smaller in the y-direction than in the x-direction. We correct for this fact by dividing the distance by the lattice distance in that direction.

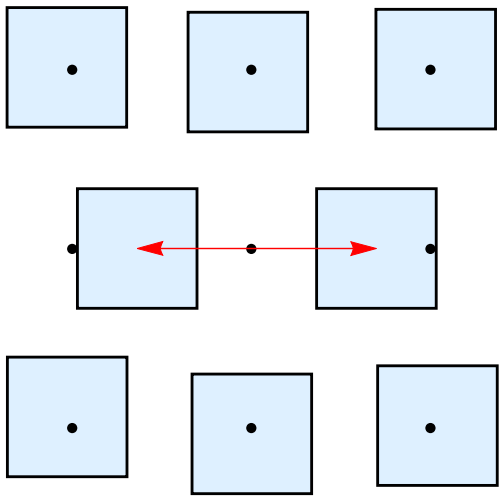

Figure 3.3.2: Cubic particles around a vacancy. The direction of the defect is equal to the horizontal direction, because the two particles around the vacancy are closest to each other in that direction.

In Chapter 5 we discuss the results of the vacancy analysis.

Chapter 4

Results: Elastic Constants

Simple cubic (sc) lattices are extremely rare. The interaction potential between the atoms in the crystal must be just right in order for an sc lattice to be stable. A typical curve for the potential function $\psi(r^2)$ is shown in Fig. 4.0.1 [30], which has a minimum at ρ_0, where the attractive and repulsive forces are in balance. Beyond the inflection point, the second derivative of the potential ψ changes sign. If the next nearest neighbour of a central atom falls beyond this point, it generally means that the distance between the next nearest neighbour and the nearest neighbour is larger than the distance between the inflection point and ρ_0. Born argued that in that case, the sc and body centred cubic (bcc) crystals are unstable [30]. Since that distance is larger for the bcc, this structure has a better chance of being stable than the single cubic structure. In fact, the only known stable sc crystal that has a single atom basis is the alpha form of Polonium, owing partly to its large mass [12].

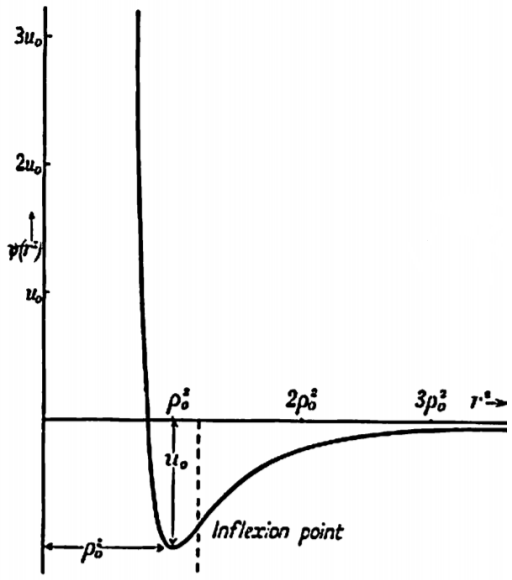

Figure 4.0.1: Typical shape of the interaction potential in a crystal as a function of the squared distance between particles r^2. The first nearest neighbour usually lies very near to the minimum at ρ_0 (taken from Ref. [30]).

Born's results were based on atomic crystals, whereas this thesis examines the behaviour of colloidal crystals. As a result of the ever advancing possibilities in synthesis, not only spherical but also monodisperse cubic particles can now be realized. Due to their shape, cubic particles form an sc lattice [11]. Moreover, results from Smallenburg [16] show that systems with these cubic particles have properties which differ vastly from a system with spherical particles. Specifically, the vacancy concentration[1], defined as $v = \frac{\#vacancies}{\#lattice\ sites}$, is very high in a system of cubes in comparison to a face centred cubic (fcc) system with spherical particles. The fcc system

[1] A vacancy is a point defect in a crystal lattice where a particle is missing. As a result the number of lattice sites is higher than the number of particles.

has a vacancy concentration of the order of 10^{-4} near the melting point [17]. Figure 4.0.2 shows the predicted vacancy concentration as a function of the packing fraction. Near the melting density of $\eta = \frac{\pi}{6}\frac{\sigma_s^3 N}{V} = 0.5$, the predicted vacancy concentration v is as high as 0.065, two orders of magnitude higher than that for the fcc system. It turns out that these defects are necessary to stabilize the sc crystal [16].

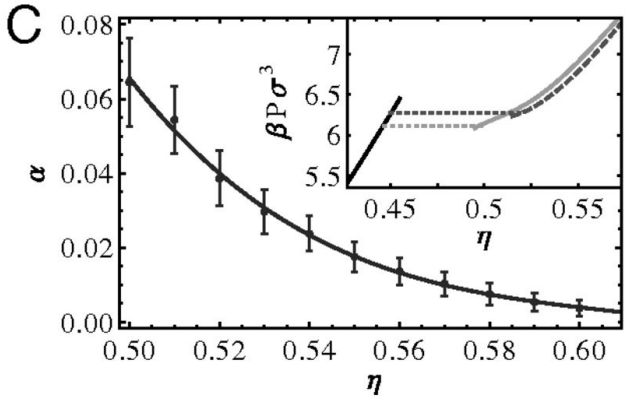

Figure 4.0.2: The net vacancy concentration a as a function of the packing fraction η. (Inset) The pressure $\beta P\sigma^3$ as a function of the packing fraction η. The fluid phase (black), and the crystal phase for a system without vacancies (black, dashed) and with a large vacancy concentration (grey, dashed) are shown. The phase transition occurs earlier for the vacancy rich system than for the system without vacancies. (taken from Ref. [16]).

This chapter discusses the relationship between the packing fraction, vacancy concentration and the elastic constants. First, the elastic constants for hard spheres without any defects are compared to literature values. Then the system of hard cubes is discussed. In the case of hard cubes, first the equation of state is explored for different vacancy concentrations. Subsequently, the elastic constants of the hard cube system are examined in the density regime of $\eta = \sigma_c^3 N/V \equiv \sigma_c^3 \rho = 0.53 - 0.6$, with σ_c the edge length of the cube, and for vacancy concentration between $v = 0.005 - 0.075$. For all hard cube systems (i.e. the undeformed, the sheared, and the stretched system), we conclude the discussion of the results with the examination of snapshots of the lattice structure. These snapshots can help us understand the behaviour of the elastic constants.

4.1 Consistency Check: Hard Spheres

There exist numerous papers and results on the elastic constants of hard spheres [18, 19]. Therefore, the hard sphere system will be used to check for consistency, while the main focus will lie on the hard cube system. The elastic constants were calculated by both methods discussed in the previous chapter. The MC and EDMD results are compared to each other and to literature values taken from Ref. [19]. The comparison is shown in Fig. 4.1.1. Both the MC and the EDMD method agree with the literature values. However, as the EDMD simulations are much more efficient, as we will explain in the following section, we chose to continue this study using only the EDMD simulations.

4.1.1 Comparison of the Two Methods

We now discuss the main differences between the two simulation techniques and the calculation methods used for the calculation of the elastic constants. The main advantage of the second calculation method (implemented in EDMD), over the first (implemented in MC) is its simulation time: it turns out that it is much shorter for the second than for the first method. This is because the system is under a constant deformation in the second method, and therefore the method does not rely on volume moves. The first method revolves around the trial of volume moves, because it extracts the elastic constants from the fluctuations of the volume from its equilibrium state. As explained in Section 3.1.2.2, the volume move is a very slow move, even with the use of a cell list. Moreover, the first method is based on volume fluctuations. A large amount of data is necessary to calculate the average fluctuations accurately. The advantage, or possible disadvantage, of this method, is that the complete elastic modulus tensor is calculated during a single simulation. Consequently, this method is very useful for crystals with a complicated structure. The structure of the crystal is needed for the initial configuration, but after the initialization, the MC method is not concerned with the structure. All information on the elastic

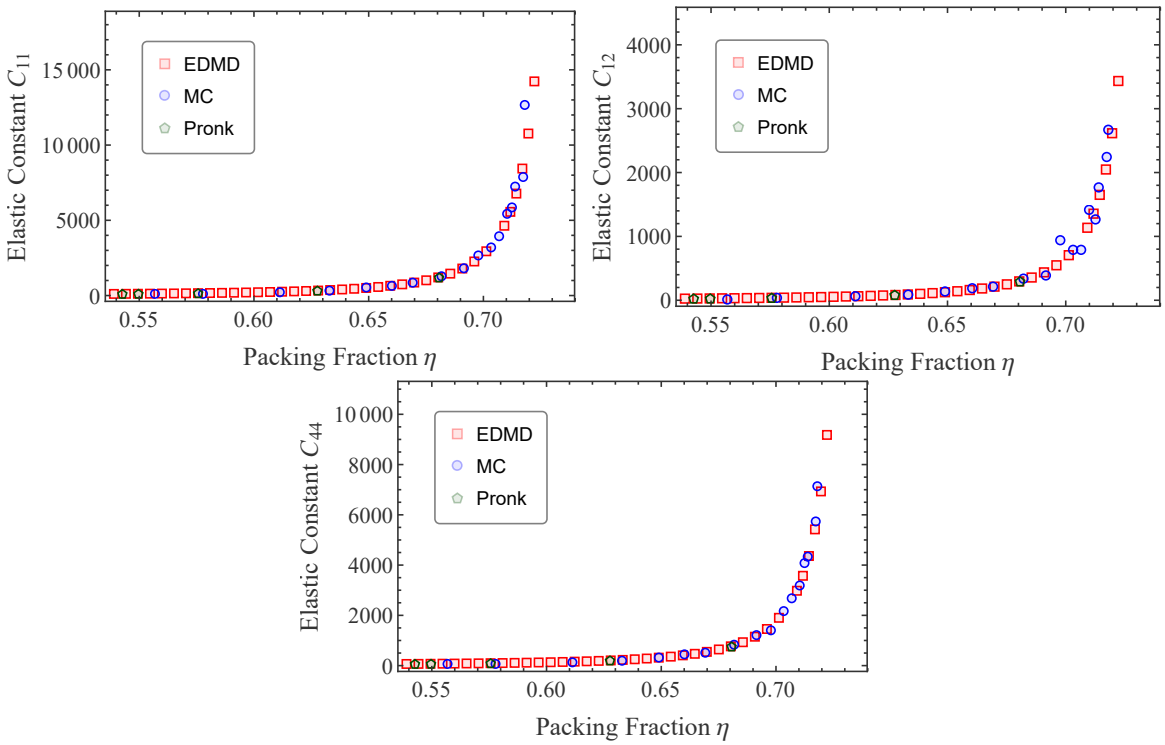

Figure 4.1.1: The three elastic constants plotted as a function of the packing fraction. The results from the Monte Carlo code (blue circles) and the EDMD results (red squares) are in good agreement with the literature values taken from Pronk [19] (green pentagons).

constants can be calculated by the measurements of the boxmatrix. This also means however, that irrelevant data is generated when we do not need the full elastic modulus tensor, which costs simulation time.

The second method does not generate irrelevant data, as it only calculates the relevant elastic constants, and not the full elastic modulus tensor. However, the symmetries of the crystal structure need to be studied in order to find the right deformation matrices. Different kind of symmetries require different deformation matrices. The fewer symmetries the structure exhibits, the more independent elastic constants there are. An equal number of different deformations must be applied to create an equal number of independent equations. Thus the second calculation method becomes ever more troublesome with an increasing number of independent elastic constants.

There are only three independent elastic constants (C_{11}, C_{12}, and C_{44}) for the cubic crystal which we study. Therefore, in this thesis the EDMD method is the more efficient simulation method of the two. For this reason, we only used the EDMD method for the calculation of the elastic constants of the hard cube system.

4.2 Hard Cubes

Having tested our method and simulations using the hard sphere system, we now examine the hard cube system. Substantially less research has been conducted on hard cubes than on hard spheres, as the synthesis of hard cubes is a more recent development and spheres are more common in nature (atoms are often approximated as spherical). In this section, the elastic constants for cubes will be explored, adding to the widely established data on systems with spherical particles. The effects of the presence of defects, which effect the stability of the system, will be discussed as well.

4.2.1 Equation of State

First we look at the equation of state of the undeformed system for various vacancy concentrations. As discussed in Section 3.2.1, the equation of state is a vital part of the calculation of C_{11} and C_{12}. Figure 4.2.1 shows the pressure as a function of the packing fraction $\eta = \sigma_c^3 \rho$, with σ_c the edge length of the cubes, for various

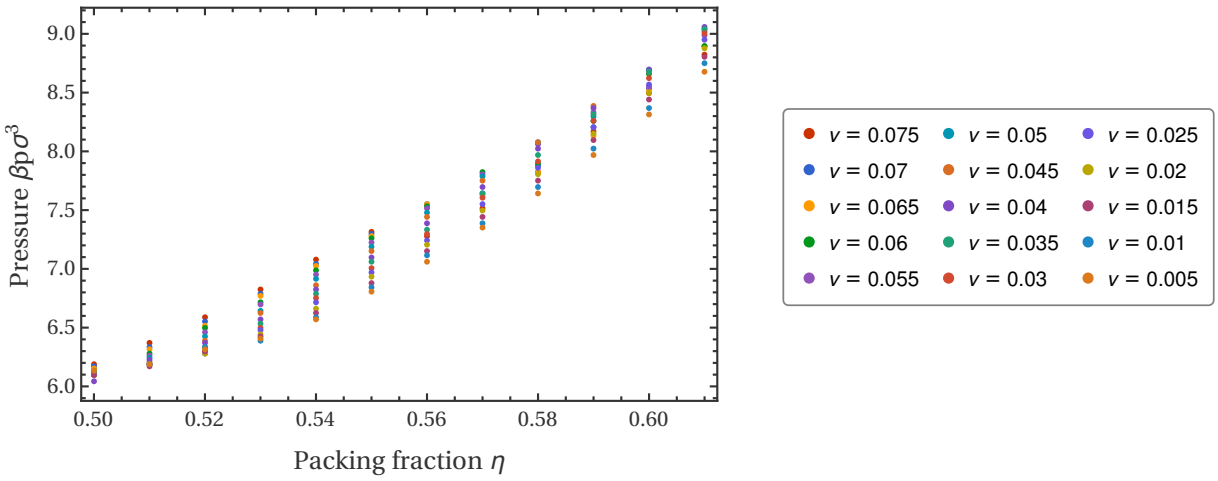

Figure 4.2.1: The pressure $\beta p\sigma_c^3$ as a function of the packing fraction η, for vacancy concentrations v between 0.005 and 0.075.

vacancy concentrations v. On first sight, there is nothing out of the ordinary: the pressure seems to increase monotonously with increasing density. However, by looking at the plots separately, a jump in the equation of state is observed at higher vacancy concentrations, see Fig. 4.2.2. This can be explained by the predicted phase behaviour of hard cubes and equilibrium vacancy concentration (Fig. 4.0.2). For the vacancy concentrations and densities where the jump occurs, the vacancy concentration is well above the ideal one for the system. Here, we suppose that the system might be reordering into a system with fewer lattice sites, due to the high vacancy number. This hypothesis will be explored further in the following section.

4.2.1.1 Lattice Structure of the Undeformed System

In order to examine the jump in the equation of state, multiple snapshots were made examining the positions of the particles. In these snapshots, the cubes' size is reduced to $0.1\sigma_c$, such that distortions of the $20 \times 20 \times 20$ lattice can be made visible. The snapshots were made at different vacancy concentrations, but all at packing fraction $\eta = 0.60$. Lowering the density while keeping the vacancy concentration constant at a high vacancy concentration should give opposite effects since the vacancy concentration will get closer to the ideal one.

Figure 4.2.3 shows the snapshots of the undeformed system, from which the equation of state was calculated. While a system with no or few vacancies results in a regular $20 \times 20 \times 20$ lattice at a density of $\sigma_c^3\rho = 0.6$, the system with the high vacancy concentration of $v = 0.06$ is distorted. Not every column in the system consists of 20 lattice sites, and the different columns are not perfectly aligned. This corresponds to the jump in the equation of state that was found earlier. From these figures we can conclude that the data of the elastic constants after the jump should not be trusted as the system is not even truly crystalline at that point. Therefore, the jump will be indicated by a red dashed line in the figures in the following sections.

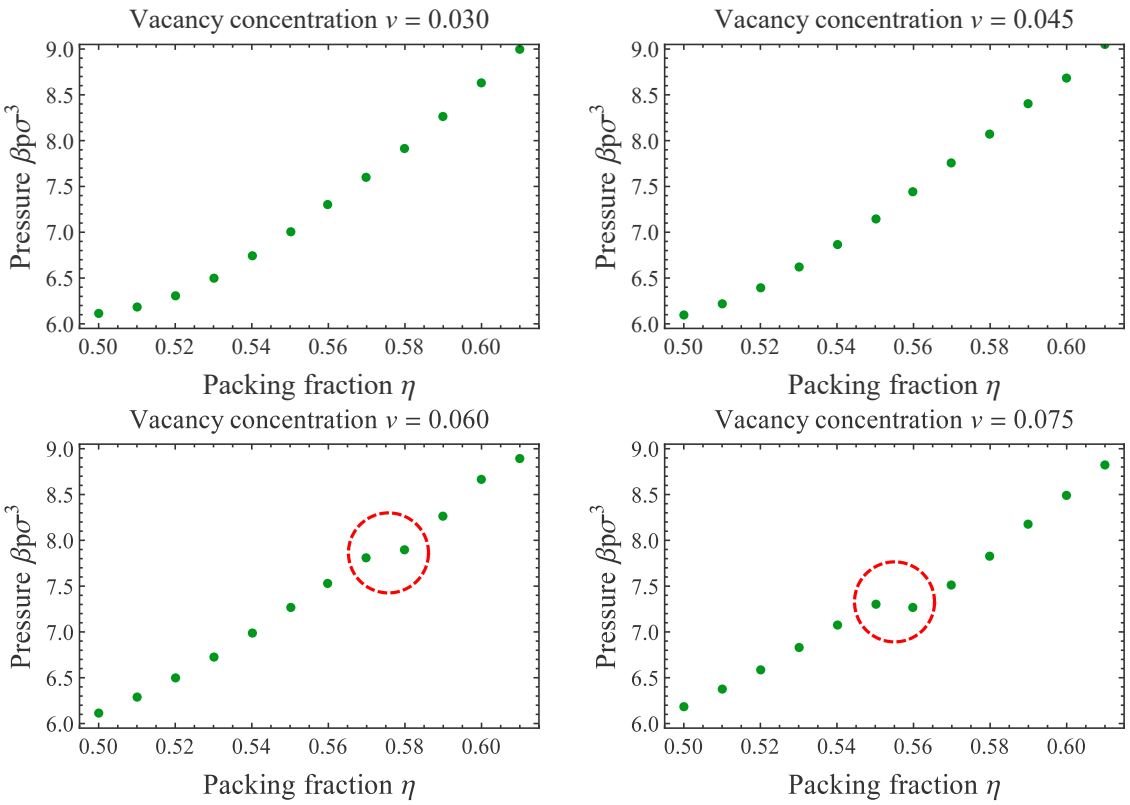

Figure 4.2.2: Pressure $\beta p\sigma_c^3$ as a function of the packing fraction η, for different vacancy concentrations v. The graphs of the high vacancy concentrations $v = 0.075$ and $v = 0.060$ exhibit a jump reaching high densities, indicated by a red dashed circle.

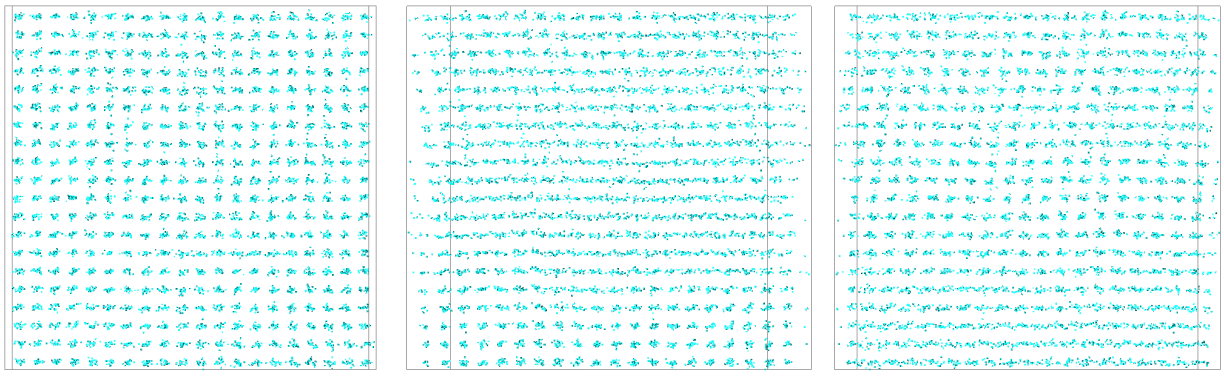

(a) (b) (c)

Figure 4.2.3: Snapshots of the undeformed system taken from different angles of the system at a density of $\sigma_c^3\rho = 0.060$; with a number of particles of $N = 7520$, such that the vacancy concentration equals $v = 0.060$. The ideal vacancy concentration at this density is approximately $v = 0.005$, far below the current one. The cubes are reduced in size to show the lattice. The lattice is shifted and is not a $20 \times 20 \times 20$ lattice through the whole system.

4.2.2 C_{11} and C_{12}

Using the results from the equation of state and the stress resulting from the application of a compression with deformation matrix:

$$D = \begin{pmatrix} 1+\delta & 0 & 0 \\ 0 & 1-\delta & 0 \\ 0 & 0 & \frac{1}{1-\delta^2} \end{pmatrix},$$

the elastic constants C_{11} and C_{12} can be calculated. Figure 4.2.4 shows the results found for different vacancy concentrations as a function of the density. Figure 4.2.5 shows the same results as a function of the vacancy concentration for different densities. In the low vacancy concentration regime, C_{11} is found to increase

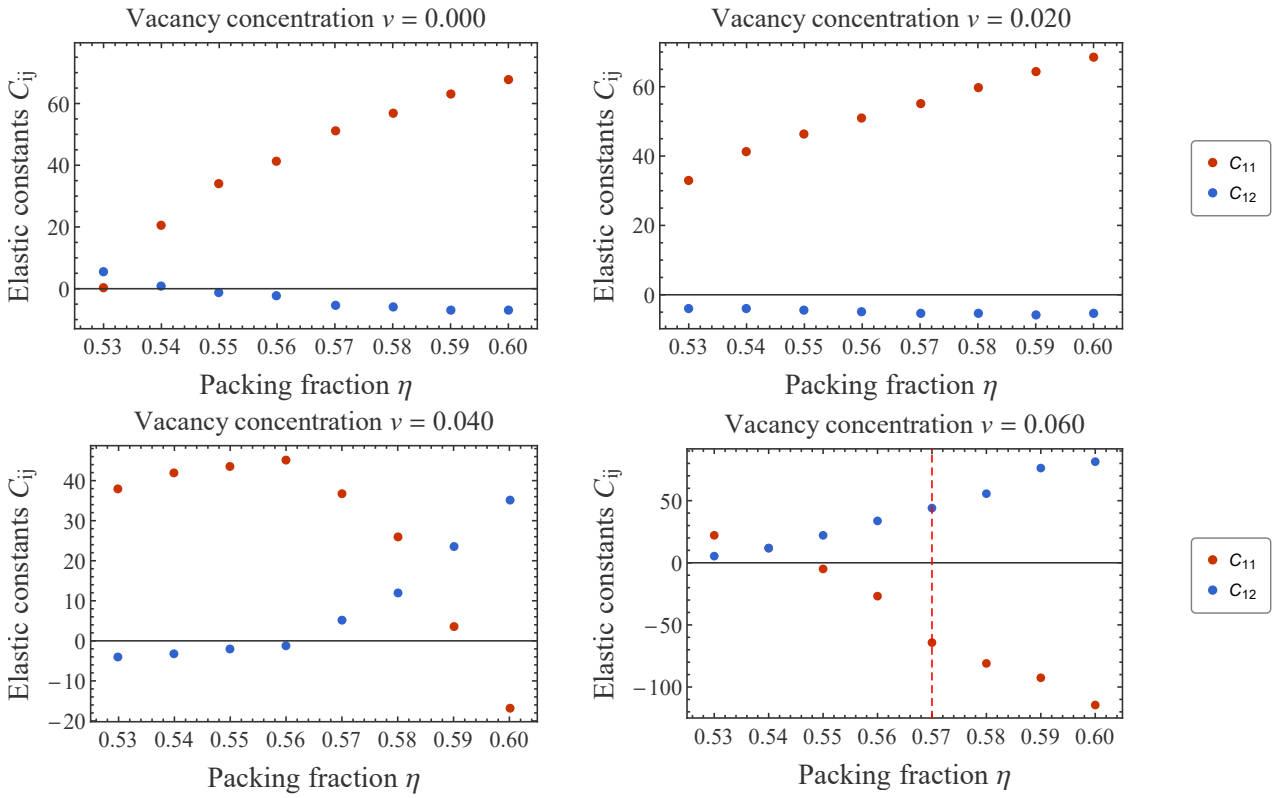

Figure 4.2.4: The elastic constants C_{11} (red) and C_{12} (blue) plotted as a function of the packing fraction η for different vacancy concentrations v. The dashed line in the last figure resembles the jump in the equation of state found earlier. C_{12} overtaking C_{11} in the lower two figures violates the Born stability principle that states that $C_{11} - C_{12} > 0$.

monotonously, while C_{12} is negative and decreases monotonously with increasing density. It should be noted that a negative C_{12} is in marked difference to what was seen for hard spheres, where C_{11}, C_{12}, and C_{44} were all positive. C_{11} resembles the internal force parallel and opposite to the applied compression. The increasing of C_{11} thus implies an increasing force counteracting this compression. The increasing of C_{11} with increasing density is not surprising because there is simply less space for the particles to move around in, and as such it becomes more difficult to compress the volume. Looking at the shape of the cubes, the negativity of C_{12} may be explained as well. Some of the cubes are rotated. As the volume is compressed in one direction, the rotated cubes could behave as a wedge, and thus spread out the cubes in the directions perpendicular to the applied compression. This would imply that compression would increase the volume in the perpendicular directions, hence the negative C_{12}.

Looking at the higher vacancy concentration regime, a different effect can be observed: C_{12} overtakes C_{11}. This contradicts the Born stability principle that $C_{11} - C_{12} > 0$. When this happens, the crystal must be unstable. As can be seen in the plot for $v = 0.06$, this happens even before the observed jump in the equation of state. However, the vacancy concentration of $v = 0.04$ is already well above the ideal vacancy concentration of $v < 0.01$ at a packing fraction of $\eta = 0.58$. Therefore, the instability does not come as a shock. Something similar can be said about elastic constants of the system with a vacancy concentration of $v = 0.0$ at a packing

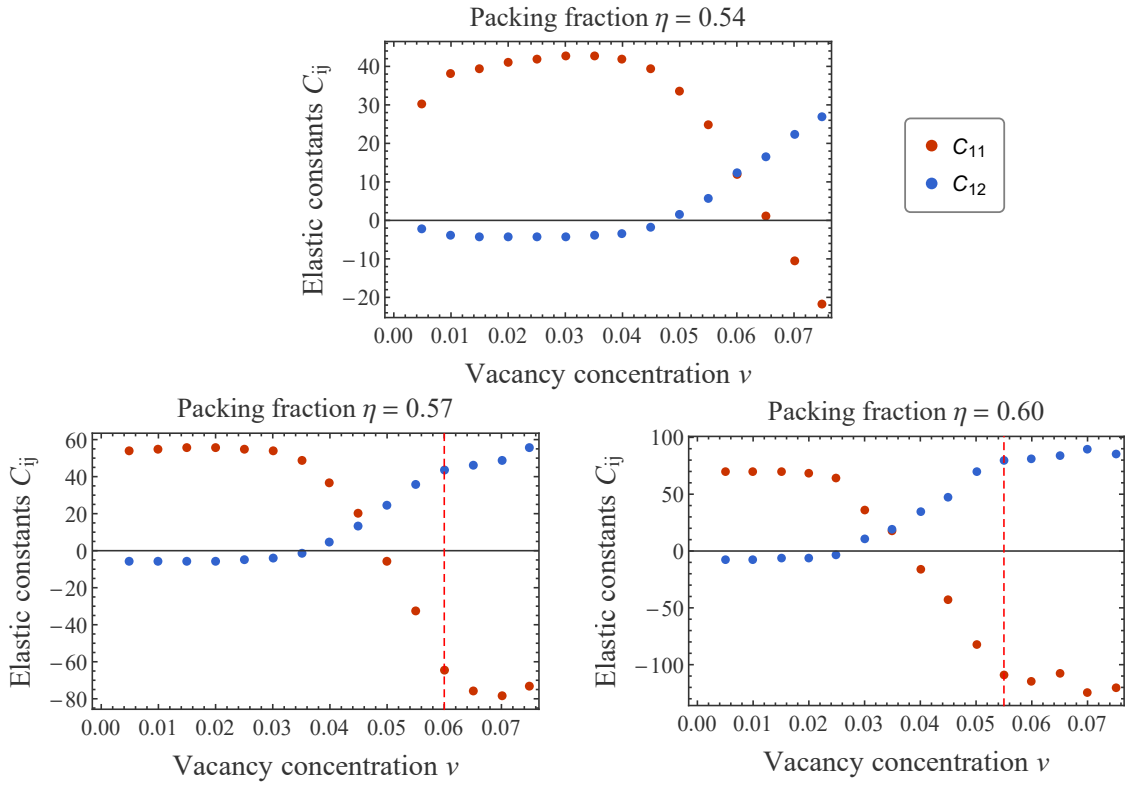

Figure 4.2.5: The elastic constants C_{11} (red) and C_{12} (blue) plotted as a function of the vacancy concentration v for different packing fractions η. The dashed line in the last two figures resembles the jump in the equation of state found earlier. C_{12} overtaking C_{11} in the lower two figures goes against the Born stability principle that states that $C_{11} - C_{12} > 0$.

of $\eta = 0.53$. There too, we see that $C_{12} > C_{11}$; the system is therefore unstable. In this case, the vacancy concentration of 0 is well below the ideal concentration, which is approximately equal to $v = 0.03$, explaining the instability. In the following section, the crystal structures will be examined in more detail at a high packing fraction by means of snapshots of the positions of the particles.

4.2.2.1 Lattice Structure of the Stretched System

Figure 4.2.6 shows the snapshots of the stretched out system, with stretchz $= 0.005\sigma_c$ (as defined in Section 3.2), at various vacancy concentrations v. Note that $v = 0.020$ corresponds to the regime where the lattice is preserved, while $v = 0.060$ shows a system that is melted to a smaller lattice ($20 \times 19 \times 20$). Fewer lattice sites are in the compressed y-direction. The vacancy concentration $v = 0.040$ is a transition state between the two lattices. This last state explains the fact that C_{12} is larger than C_{11} before the jump, as can be seen in Fig. 4.2.5. The system is in transition, and therefore indeed unstable, in which case C_{12} can actually be larger than C_{11}.

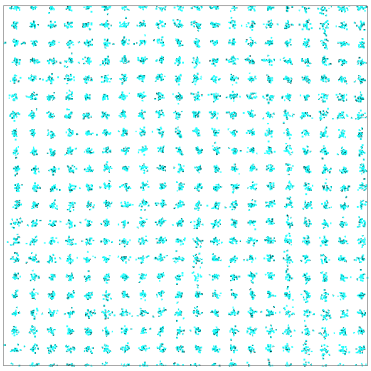

(a) $v = 0.020$, xy-plane

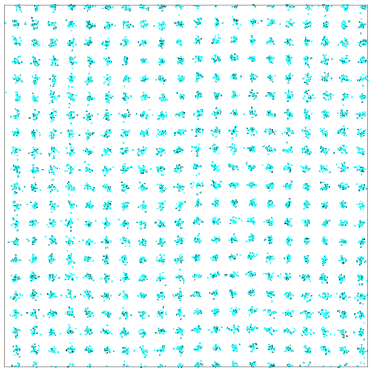

(b) $v = 0.020$, xz-plane

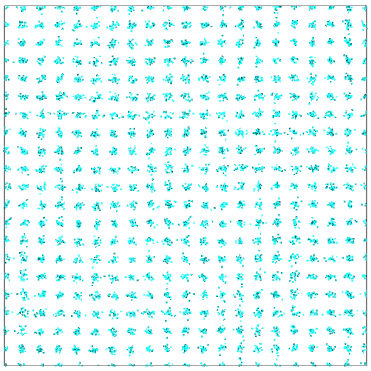

(c) $v = 0.020$, zy-plane

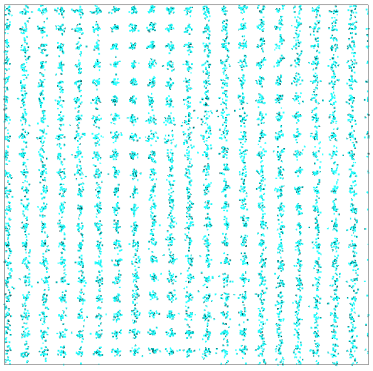

(d) $v = 0.040$, xy-plane

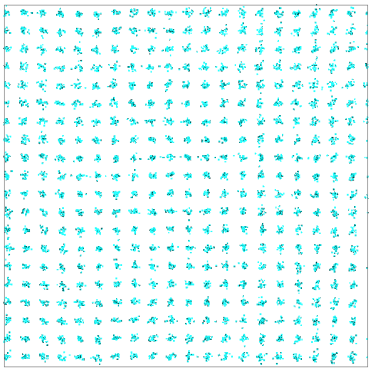

(e) $v = 0.040$, xz-plane

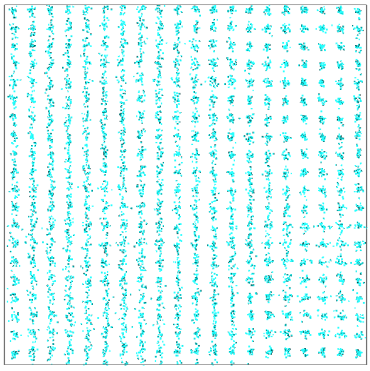

(f) $v = 0.040$, zy-plane

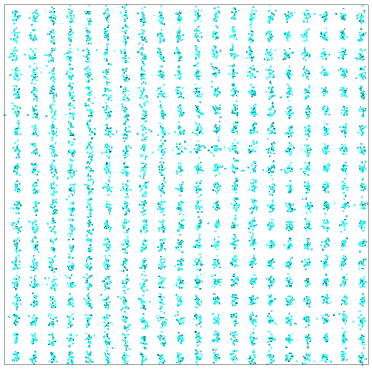

(g) $v = 0.060$, xy-plane. This plane shows a 20×19 lattice sites.

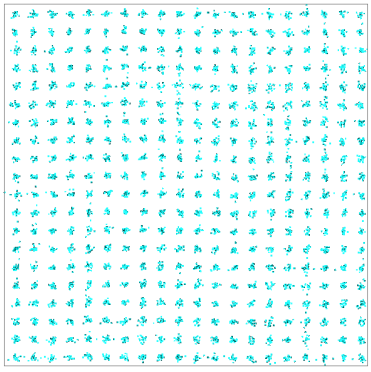

(h) $v = 0.060$, xz-plane. This plane shows a 20×20 lattice sites.

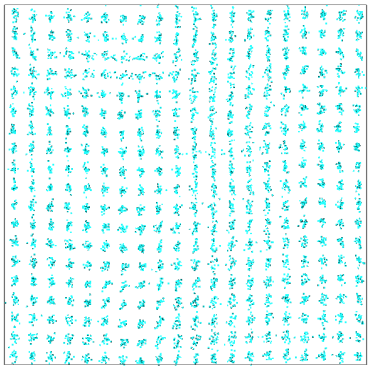

(i) $v = 0.060$, zy-plane. This plane shows a 20×19 lattice sites.

Figure 4.2.6: Snapshots from different planes of the compressed system for three different vacancy concentrations, with packing fraction $\eta = 0.6$ and stretchz $= 0.005\sigma_c$, such that the volume is compressed in the y-direction. The cubes are reduced in size to show the lattice. The upper three figures, with the lowest vacancy concentration, show a regular $20 \times 20 \times 20$ lattice. The lower three figures, which display the system with the highest vacancy concentration, show that the system has transformed from a $20 \times 20 \times 20$ to a $20 \times 19 \times 20$ lattice. The three figures in the middle (d, e, f) show a transitional state between the $20 \times 20 \times 20$ and $20 \times 19 \times 20$ lattice.

4.2.3 C_{44}

Using the stress resulting from the applied shear with the corresponding deformation matrix:

$$D = \begin{pmatrix} 1 & \delta & 0 \\ \delta & 1 & 0 \\ 0 & 0 & \frac{1}{1-\delta^2} \end{pmatrix},$$

the elastic constant C_{44} was calculated. Figure 4.2.7 shows the results found for different vacancy concentrations as a function of the density. Figure 4.2.8 shows the same results as a function of the vacancy concentration for different densities. The main trend is that as the density and/or the vacancy concentration increase, C_{44} becomes larger as well. Both effects are reasonable. Due to the shape of the cubes, increasing the density makes it increasingly difficult to shear the system, because it becomes more likely that rotated cubes interfere with each other, resisting the shear. A higher vacancy concentration could cause difficulties for shearing the system in another way: The particles around the vacancies have more freedom to move away from their lattice site, causing a distortion in the columns of the vacancies and thus blocking the shear force. This effect can be seen in the snapshots of the systems, which will be discussed in the following section.

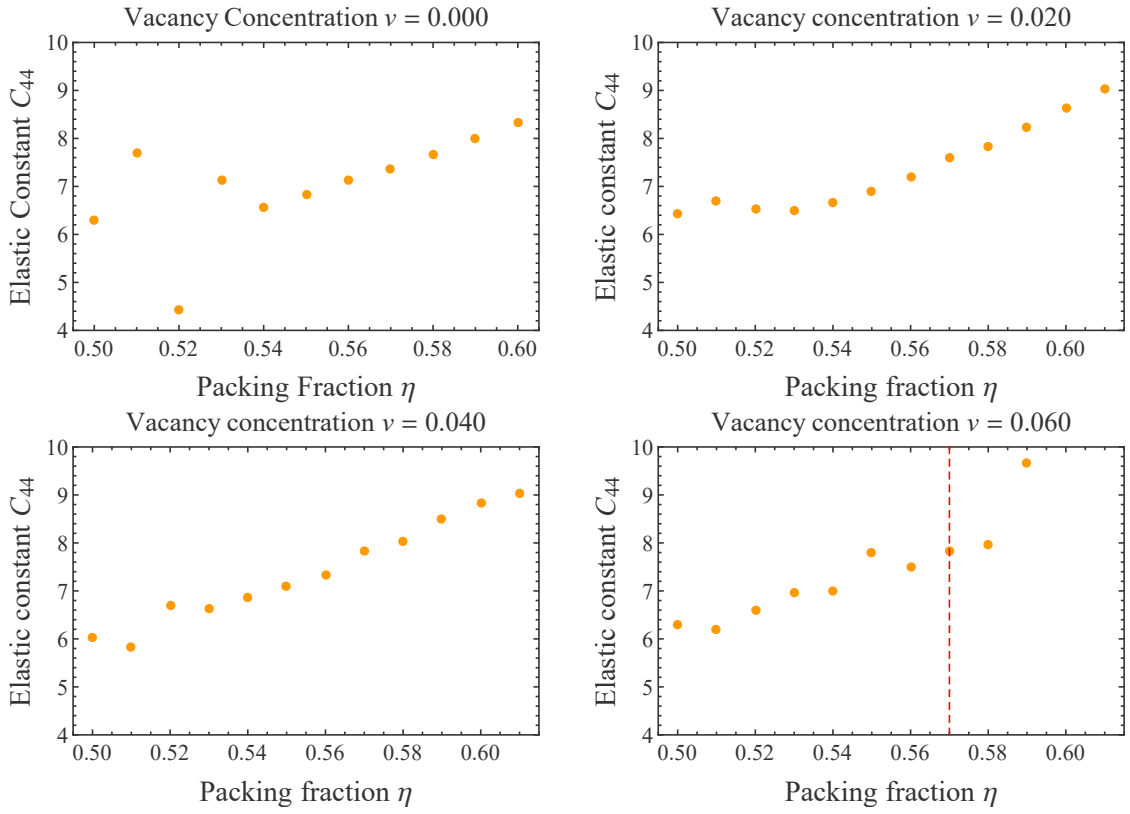

Figure 4.2.7: The elastic constant C_{44} plotted as a function of the packing fraction η for different vacancy concentrations v. The dashed line in the last figure resembles the jump in the equation of state found earlier.

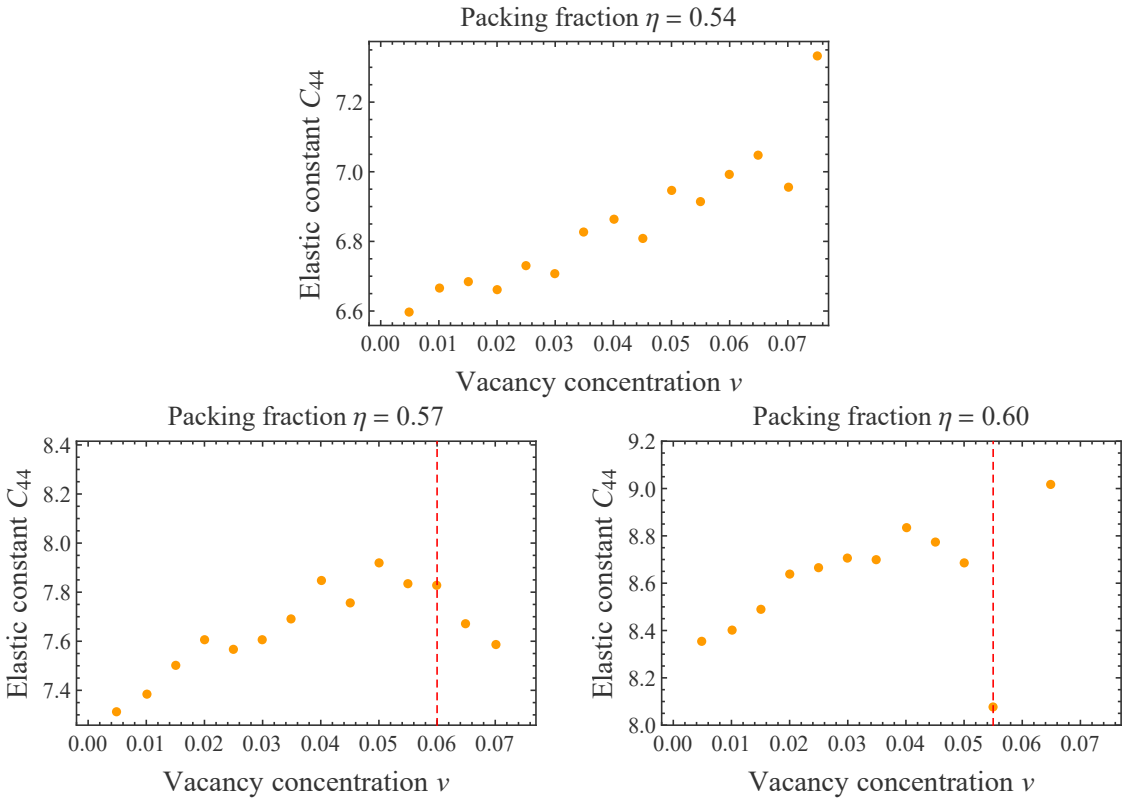

Figure 4.2.8: The elastic constant C_{44} plotted as a function of the vacancy concentration v for different packing fractions η. The dashed line in the last two figures resembles the jump in the equation of state found earlier.

4.2.3.1 Lattice Structure of the Sheared system

Figure 4.2.9 shows the snapshots of the sheared system, with shiftx $= 0.005\sigma_c$ at various vacancy concentrations. As predicted in Section 4.2.3, the lattice becomes less regular going from a vacancy concentration of $v = 0.02$ to $v = 0.04$. At the high vacancy concentration of $v = 0.06$, the lattice has even shifted, aligning with the shear force put on the system.

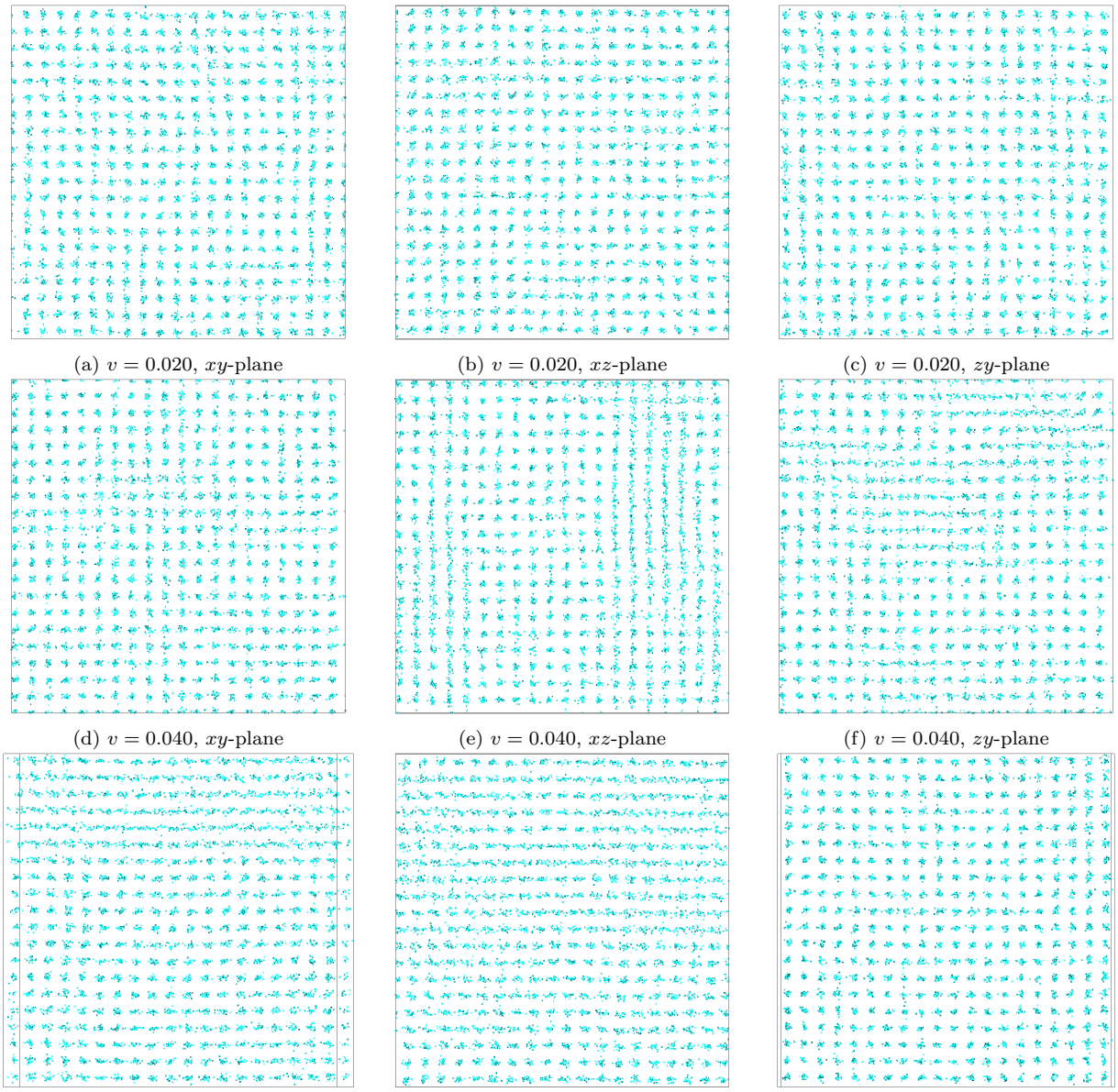

(a) $v = 0.020$, xy-plane (b) $v = 0.020$, xz-plane (c) $v = 0.020$, zy-plane

(d) $v = 0.040$, xy-plane (e) $v = 0.040$, xz-plane (f) $v = 0.040$, zy-plane

(g) $v = 0.060$, xy-plane. This plane shows a 19×20 lattice sites.

(h) $v = 0.060$, xz-plane. This plane shows a 19×20 lattice sites.

(i) $v = 0.060$, zy-plane. This plane shows a 20×20 lattice sites.

Figure 4.2.9: Snapshots from different planes of the sheared system for three different vacancy concentrations, with packing fraction $\eta = 0.6$ and shiftx$= 0.005\sigma_c$. The cubes are reduced in size to show the positional order of the cubes. The upper three figures, with the lowest vacancy concentration, show a regular $20 \times 20 \times 20$ lattice. The lower three figures, which display the system with the highest vacancy concentration, show that the system has transformed from a $20 \times 20 \times 20$ to a $19 \times 20 \times 20$ lattice. The three figures in the middle (d, e, f) show a transitional state between the $20 \times 20 \times 20$ and $20 \times 19 \times 20$ lattice.

4.3 Conclusion

We tested our elastic constants by comparing them to literature values. We found good agreement for both the MC and the EDMD simulations. We then calculated the elastic constants for the hard cube system for different packing fractions and vacancy concentrations using the EDMD method. We found that the general trend for the elastic constants is that C_{11} and C_{44} increase and C_{12} decreases as a function of both the density and the vacancy concentration. At a certain density and vacancy concentration, the derivative of C_{11} and C_{12} changes sign, causing C_{12} to overtake C_{11}. As this is a sign of instability, the snapshots of the systems were examined, and large distortions of the cubic $20 \times 20 \times 20$ lattice were found at higher vacancy concentrations and densities.

The vacancies in hard cubes are known to have an abnormal structure: they form elongated 1D chains of displaced particles [16]. It would be interesting to see how the deformations associated with elastic constants interact with the defect structure. In the next chapter we place the system under strains in the non-linear regime. We locate the vacancies and calculate the direction of the defects, investigating the correlation between the deformation and the direction.

Chapter 5

Results: Tracking Vacancies

Monovacancies in hard sphere systems have been researched extensively. Although vacancies appear in low concentrations in the fcc crystal [17], they have a large effect on material properties: for example magnetism [31], and mechanic strength [32]. In 2004, Kwak studied the effects of strain on the monovacancy concentration in the fcc hard sphere crystal [33]. He found that the monovacancy concentration increased significantly for the shear and expansion-contraction deformations. The effect was more apparent for the expansion-contraction deformation than for the shear deformation. The effect enhances for increasing densities.

In 2012, Smallenburg studied the vacancy concentration for hard cube crystals [16]. As said in Chapter 4, the ideal vacancy concentration in hard cube crystals is much higher than for hard sphere systems. Moreover, the vacancies form elongated defects in the shape of large 1D chains of displaced particles, see Fig. 5.0.1. As

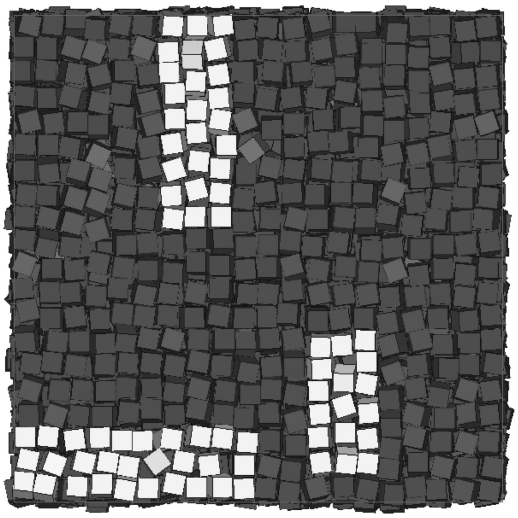

Figure 5.0.1: A snapshot of a crystal with a vacancy concentration of $v = 0.016$. Three defects and their neighbouring particles are highlighted. In the uppermost defect, six particles share seven lattice sites. In the leftmost defect, seven particles share eight lattice sites. In the rightmost defect, three particles share four lattice sites (taken from Ref. [16]).

Kwak found a correlation between the deformation of the fcc crystal and the concentration of the monovacancies, there is a good chance that there exists a correlation for the cubic particles as well. We will not study the concentration of the vacancies, but rather the direction of the defects.

In this chapter we will examine the correlation between the deformation of the crystal and the direction of its defects. First we will test our method for the undeformed system. Subsequently, we examine the defects in a sheared system for various shiftx and in a stretched system for various stretchz.

5.1 Defect Direction

In order to study the correlation between the direction of the defects and the deformation of the system, we applied non-linear deformations, for a low vacancy concentration. The direction of the defects was determined using the method described in Section 3.3. If defects align with the deformation, either parallel or perpendicular to the applied force, this might happen on a smaller scale in the linear regime as well. If no effect can be observed, it can be concluded that there will be no alignment in the linear regime either. Both the shear and the stretch deformation were examined.

We first check the undeformed system, to ensure that our method is working correctly. Clearly for the undeformed system we do not expect any preferential direction. As shown in Fig. 5.1.1, indeed no preferred direction is found. This is a reasonable indication that our method is working correctly.

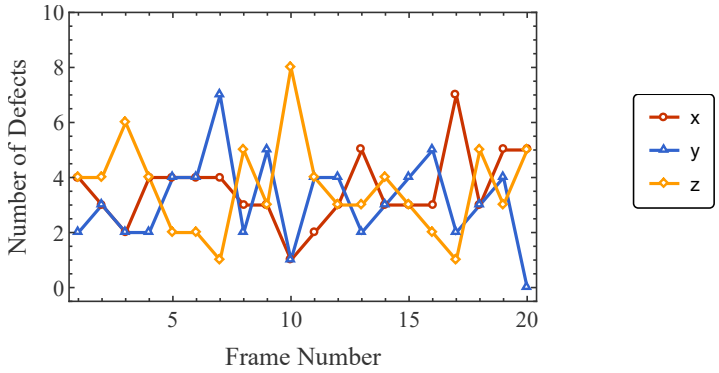

Figure 5.1.1: Number of defects counted aligned with directions x, y, and z in an undeformed system. Every frame is taken after 20.000 steps. The number of lattice sites is 8000, the vacancy concentration is $v = 1.25 \cdot 10^{-4}$, and the packing fraction equals $\eta = 0.70$.

The results for the sheared system are shown in Fig. 5.1.2 for different values of shiftx. No preferred direction can be observed. We do note that the total number of vacancies is larger than 10, the initial number of vacancies. This is most apparent for the largest value of shiftx.

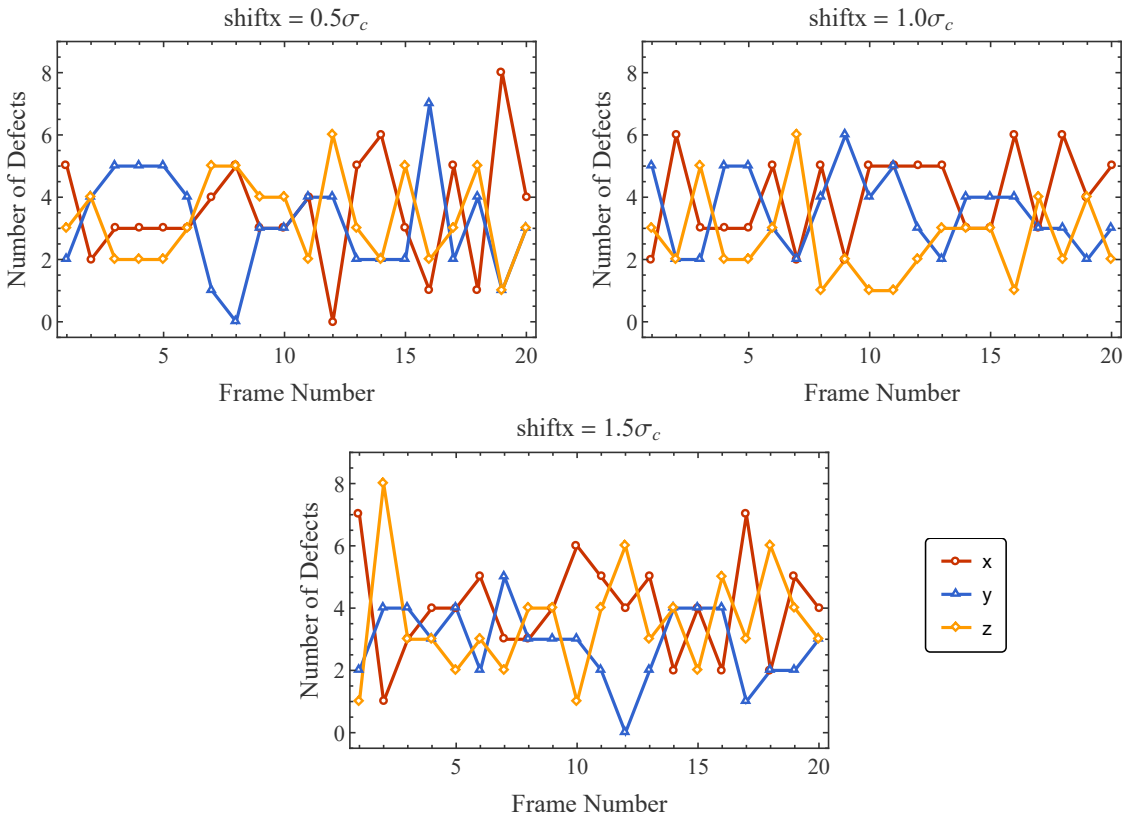

Figure 5.1.2: Number of defects aligned with directions x, y, and z. Every frame is taken after 20.000 steps. The system is sheared with different values for shiftx. The number of lattice sites is 8000, the vacancy concentration is $v = 1.25 \cdot 10^{-4}$, and the packing fraction equals $\eta = 0.70$.

The results for the stretched system are shown in Fig. 5.1.3, for different values of stretchz. The direction in which the system is compressed (the y-direction), is clearly the preferred direction of the defects. This becomes more apparent with increasing values for stretchz. The total number of vacancies is occasionally larger than the initial 10 for stretchz $= 0.03\sigma_c$. For stretchz $= 0.05\sigma_c$, the number of vacancies clearly grows, and the x-direction is preferred over the z-direction. For this high value of stretchz, the distance between the lattice sites are equal to:

$$\text{lat}_x = 1.18207 \cdot \sigma_c, \tag{5.1.1}$$
$$\text{lat}_y = 1.06949 \cdot \sigma_c, \tag{5.1.2}$$
$$\text{lat}_z = 1.12860 \cdot \sigma_c. \tag{5.1.3}$$

We see that the distance between two lattice sites in the y-direction is barely larger than the size of a particle. Around a vacancy, the particles gain more freedom of movement, and it makes sense that they move in the y-direction. The particles have a lot of freedom in the x-direction. As particles move around in the x-direction, extra vacancies can be created, which would then be aligned in the x-direction. When a vacancy is created, more space is created around that vacancy for the particles to move in the y-direction, such that the defect can change direction, explaining the growing number of defects in the y-direction: the system melts locally to a $20 \times 19 \times 20$ lattice.

The fact that the stretching of the system has more effect on the defects than the shearing is in good agreement with the results found by Kwak [33].

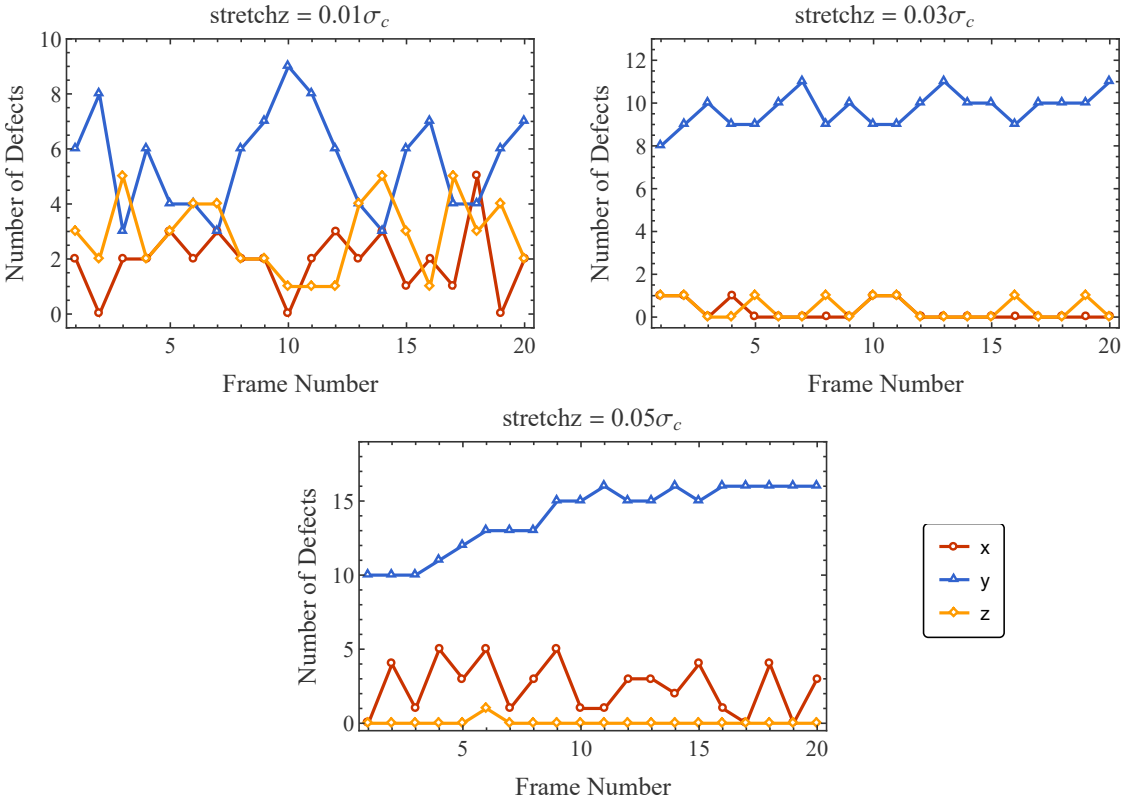

Figure 5.1.3: Number of defects counted aligned with directions x, y, and z. Every frame is taken after 20.000 steps. The system is stretched, with different values for stretchz. The number of lattice sites is 8000, the vacancy concentration is $v = 1.25 \cdot 10^{-4}$, and the packing fraction equals $\eta = 0.70$. The compressed y-direction is clearly the preferred direction of the defects. This preference becomes stronger with increasing stretchz.

5.2 Conclusion

We have studied two different deformations (shear and stretch) in the non-linear regime on a system with a packing fraction of $\eta = 0.70$, 8000 lattice sites, and a vacancy concentration of $v = 1.25 \cdot 10^{-4}$ (i.e. 10 vacancies). We calculated the direction of the defects caused by the vacancies. For the sheared system, no correlation was found between the direction of the defects and the deformation. The number of vacancies did exceed the initial number of vacancies occasionally. For the stretched system, we found that the defects aligned with the compressed y-direction. For the largest value of stretchz examined, we found that the number of vacancies grows over time. The new defects also took on the y-direction.

Chapter 6

Summary and Outlook

For the face centred cubic crystal with hard sphere particles, we have calculated the elastic constants using two simulation techniques: Monte Carlo and Event Driven Molecular Dynamics. We have compared the results to literature values from Pronk [19] and found good agreement with both the MC and the EDMD results. We continued using the EDMD method for the cubic particles for efficiency reasons. We calculated the elastic constants for different vacancy concentrations v and packing fractions η. We found that C_{11} and C_{44} are both positive, and increase with both increasing vacancy concentration and with increasing density. C_{12} was found to be negative for the cubic particles, which is in marked difference to the system with spherical particles. C_{12} decreases as a function of both the vacancy concentration and the packing fraction. At high vacancy concentrations, the cubic particle system disobeys the Born stability criterium of $C_{11} - C_{12} > 0$ [30]. The snapshots of the system at those high values showed the instability as well. This result agrees with the predicted vacancy concentrations of Smallenburg [16] (see Fig. 4.0.2). The equilibrium vacancy concentration is rather low at high densities. A high vacancy concentration at a high density could therefore destabilize the crystal.

Subsequently we examined the correlation between the direction of defects around the vacancies and the deformation of the crystal. First, we tracked the direction of the defects for an undeformed system to test our method. As expected, no preferred direction was found. Second, we applied two deformations in the non-linear regime: the shear and the stretch deformation. In the case of the shear deformation, we found no preferred direction. The number of vacancies did increase slightly, in correspondence with the results from Kwak for spherical particles [33]. The stretched system does have a preferred direction for the defects, namely the direction in which the system was compressed. This effect becomes more apparent for larger deformations. At the largest deformation examined, the number of vacancies became larger over time. The defects created by these new vacancies also took on the compressed direction. Consequently, the colloidal crystal exhibits local melting.

We conclude this thesis by addressing some possibilities for further research. First of all, it could be useful to improve the efficiency of the Monte Carlo simulations. In Section 4.1.1, we explained that the Monte Carlo method is more versatile, but the EDMD method proved to be more efficient. Therefore, we chose to abandon the Monte Carlo method in this thesis. However, the Monte Carlo simulation method can be made much more efficient by implementing clusters moves. The volume cluster algorithm, suggested by Almarza et. al., generates an equation of state that is very close to the Speedy equation of state [34]. The idea behind the algorithm is that during a volume move, only the distances between the different clusters change, while the distances between particles within the same cluster stay constant. Therefore the particles within the same cluster will not overlap, and only the overlap between neighbouring clusters should be checked. The volume move is the slowest move in our Monte Carlo simulations, hence the efficiency of the simulations can be improved significantly by improving the efficiency of the volume move.

When the simulation time of the Monte Carlo simulation can be reduced sufficiently, the method can be used for other systems than the hard sphere system. Filion studied the self-assembly of several binary hard sphere systems, including a colloidal interstitial solid [35, 36]. This solid is an fcc crystal of large spheres, where a fraction of the octahedral holes are filled with smaller spheres. Surprisingly, the diffusion of the small particles between neighbouring holes increases with increasing density of these small spheres. We found that the vacancy concentration of the hard cube system increases when a deformation is applied, which is the same effect as was found for hard spheres by Kwak [33]. It would be interesting to examine whether the diffusion of

the small spheres of the interstitial solid is affected by deformations as well. Furthermore, one could examine the effect of the diffusion on the elastic constants of the system.

Another interesting line of inquiry is the dependency of the elastic constants on the particle shape. As said earlier, the elastic constant C_{12} behaves differently for cubes than for spheres. It is possible that this difference is simply caused by the difference in lattice structure: the hard sphere system is an fcc crystal, whereas the hard cubes arrange in a sc lattice. Furthermore, the vacancy concentration in the fcc crystal is much lower than that of the sc crystal [16, 17]. Therefore, we want to study a particle system with similar phase and vacancy behaviour and similar structure as the structure of the hard cubes, but with a different shape than the cube. Van Damme studied such a particle in his master thesis: the slanted cube [37]. Interestingly, he found no difference in the vacancy concentration of the slanted cube system for different slant angles (including an angle of 90°, which results in a regular cube). In our discussion of the dependency of the elastic constants on the vacancy concentration, we did mention the possible influence of the shape of the cube. We would expect a different behaviour for the slanted cubes under deformation, especially for the shear deformation. It could also be possible that shearing the system in different directions would have different effects, as the slanted cubes have a different symmetry than the regular cubes.

Chapter 7

Bibliography

[1] J. Pokluda and P. Šandera, *Micromechanisms of Fracture and Fatigue: In a Multi-scale Context*. Springer, 2010.

[2] A. E. H. Love, *A Treatise on the Mathematical Theory of Elasticity*. Cambridge University Press, 1906.

[3] L. D. Landau and E. M. Lifshitz, *Theory of Elasticity 3rd edition*. Elsevier, 1986.

[4] W. Ostwald, *An Introduction to Theory and Applied Colloid Chemistry*. John Wiley & Sons, Inc., 1917.

[5] C. G. De Kruif, W. J. Briels, R. P. May, and A. Vrij, "Hard-Sphere Colloidal Silica Dispersions. The Structure Factor Determined with SANS," *Langmuir*, vol. 4, no. 3, pp. 668–676, 1988.

[6] A. Vrij, J. W. Jansen, J. K. G. Dhont, C. Pathmamanoharan, M. M. Kops-Werkhoven, and H. M. Fijnaut, "Light scattering of colloidal dispersions in non-polar solvents at finite concentrations. Silica spheres as model particles for hard-sphere interactions," *Faraday Discussions of the Chemical Society*, vol. 76, no. 0, p. 19, 1983.

[7] C. G. Kruif, E. M. F. Iersel, and A. Vrij, "Hard sphere colloidal dispersions: Viscosity as a function of shear rate and volume fraction," *The Journal of Chemical Physics*, vol. 83, pp. 4717–4725, nov 1985.

[8] J. A. Champion, Y. K. Katare, and S. Mitragotri, "Particle Shape: A New Design Parameter for Micro- and Nanoscale Drug Delivery Carriers," *J. Control Release*, vol. 121, pp. 3–9, aug 2014.

[9] C. J. Murphy, T. K. Sau, A. M. Gole, C. J. Orendorff, J. Gao, L. Gou, S. E. Hunyadi, and T. Li, "Anisotropic Metal Nanoparticles: Synthesis, Assembly, and Optical Applications," *Journal of Physical Chemistry B*, vol. 109, pp. 13857–13870, jul 2005.

[10] S. Torquato and F. H. Stillinger, "Jammed hard-particle packings: From Kepler to Bernal and beyond," *Reviews of Modern Physics*, vol. 82, pp. 2633–2672, sep 2010.

[11] L. Rossi, S. Sacanna, W. T. M. Irvine, P. M. Chaikin, D. J. Pine, and A. P. Philipse, "Cubic crystals from cubic colloids," *Soft Matter*, vol. 7, no. 9, p. 4139, 2011.

[12] D. Legut, M. Friák, and M. Šob, "Why Is Polonium Simple Cubic and So Highly Anisotropic?," *Physical Review Letters*, vol. 99, no. 1, 2007.

[13] E. Jagla, "Melting of hard cubes," *Physical Review E*, vol. 58, pp. 4701–4705, oct 1998.

[14] U. Agarwal and F. A. Escobedo, "Mesophase behaviour of polyhedral particles.," *Nature materials*, vol. 10, pp. 230–235, mar 2011.

[15] H. Malmir, M. Sahimi, and M. R. R. Tabar, "Microstructural characterization of random packings of cubic particles," *Scientific Reports*, vol. 6, p. 35024, oct 2016.

[16] F. Smallenburg, L. Filion, M. Marechal, and M. Dijkstra, "Vacancy-stabilized crystalline order in hard cubes.," *Proceedings of the National Academy of Sciences of the United States of America*, vol. 109, no. 44, pp. 17886–90, 2012.

[17] C. H. Bennett and B. J. Alder, "Studies in Molecular Dynamics. IX. Vacancies in Hard Sphere Crystals," *The Journal of Chemical Physics*, vol. 54, no. 11, p. 4796, 1971.

[18] K. J. Runge and G. V. Chester, "Monte Carlo determination of the elastic constants of the hard-sphere solid," *Physical Review A*, vol. 36, pp. 4852–4858, nov 1987.

[19] S. Pronk and D. Frenkel, "Large Difference in the Elastic Properties of fcc and hcp Hard-Sphere Crystals.," *Physical review letters*, vol. 90, no. 25 Pt 1, p. 255501, 2003.

[20] W. Voigt, "Theoretical studies of the elastic behaviour of crystals," *Abh Gesch Wissenshaften*, vol. 34, pp. 3–52, 1887.

[21] A. A. Gusev, M. M. Zehnder, and U. W. Suter, "Fluctuation formula for elastic constants," *Physical Review B*, vol. 54, no. 1, pp. 1–4, 1996.

[22] M. Parrinello and a. Rahman, "Strain fluctuations and elastic constants," *The Journal of Chemical Physics*, vol. 76, no. 1982, p. 2662, 1982.

[23] M. E. J. Newman and G. T. Barkema, *Monte Carlo Methods in Statistical Physics*. Oxford University Press, 1999.

[24] B. J. Alder and T. E. Wainwright, "Studies in Molecular Dynamics. I. General Method," *The Journal of Chemical Physics*, vol. 31, pp. 459–466, aug 1959.

[25] M. Wilson and M. Allen, "Computer simulation study of liquid crystal formation in a semi-flexible system of linked hard spheres," *Molecular Physics*, vol. 80, pp. 277–295, oct 1993.

[26] D. C. Rapaport, "The Event-Driven Approach to N -Body Simulation," *Progress of Theoretical Physics*, no. 178, pp. 5–14, 2009.

[27] R. J. Speedy, "Pressure and entropy of hard-sphere crystals," *Journal of Physics: Condensed Matter*, vol. 10, pp. 4387–4391, may 1998.

[28] S. Boyd and L. Vandenberghe, *Convex Optimization*, vol. 25. Cambridge University Press, 2004.

[29] M. Marechal, U. Zimmermann, and H. Löwen, "Freezing of parallel hard cubes with rounded edges," *Journal of Chemical Physics*, vol. 136, no. 14, 2012.

[30] M. Born and K. Huang, *Dynamical Theory of Crystal Lattices*. Oxford University Press, 1954.

[31] R. J. Gambino, R. R. Ruf, and P. Fumagalli, "The role of vacancies in the magnetic and magneto-optic properties of Tb-doped EuO and EuS films," *Journal of Applied Physics*, vol. 73, pp. 6109–6111, may 1993.

[32] S.-H. Jhi, S. G. Louie, M. L. Cohen, and J. Ihm, "Vacancy Hardening and Softening in Transition Metal Carbides and Nitrides," *Physical Review Letters*, vol. 86, pp. 3348–3351, apr 2001.

[33] S. K. Kwak and D. A. Kofke, "Elastic constants and the effect of strain on monovacancy concentration in fee hard-sphere crystals," *Physical Review B - Condensed Matter and Materials Physics*, vol. 70, no. 21, pp. 1–6, 2004.

[34] N. G. Almarza, "A cluster algorithm for Monte Carlo simulation at constant pressure," *Journal of Chemical Physics*, vol. 130, no. 18, 2009.

[35] L. Filion, M. Hermes, R. Ni, E. C. M. Vermolen, A. Kuijk, C. G. Christova, J. C. P. Stiefelhagen, T. Vissers, A. Van Blaaderen, and M. Dijkstra, "Self-Assembly of a Colloidal Interstitial Solid with Tunable Sublattice Doping," *Physical Review Letters*, vol. 107, no. 16, pp. 1–4, 2011.

[36] L. C. Filion, "Self-assembly in colloidal hard-sphere systems," *Thesis*, 2011.

[37] R. van Damme, "Phase and vacancy behaviour of hard slanted cubes : a quantitative analysis on the influence of shape," *Master Thesis*, 2016.

Appendix A

Limitations to Approximation of the Strain Tensor

For small deformations in bodies of which no dimension is small, the last term from Eq. 2.1.2 can be omitted since the derivatives of the displacement vector will be small as well. Then the strain tensor becomes [3]:

$$\epsilon_{ij} = \frac{1}{2}\left(\frac{\partial u_i}{\partial x_j} + \frac{\partial u_j}{\partial x_i}\right). \tag{A.0.1}$$

There are certain limitations to the reasoning above. As mentioned, the double derivative term in the strain tensor can be neglected in bodies that are large in all dimensions. For a small deformation, the strain will be small as well, because they give the relative change in length in the body [3]. This does not mean that the displacement vector is small as well. Figure A.0.1 shows a deflected thin rod. The deformation is small, but the two ends of the rod are displaced significantly from their original position. The displacement vector $u_i = x_i' - x_i$ is therefore large. In bodies of which no dimension is small, this cannot happen. A significantly large displacement vector can then only be the result of a large deformation. This thesis only discusses bodies of this last category.

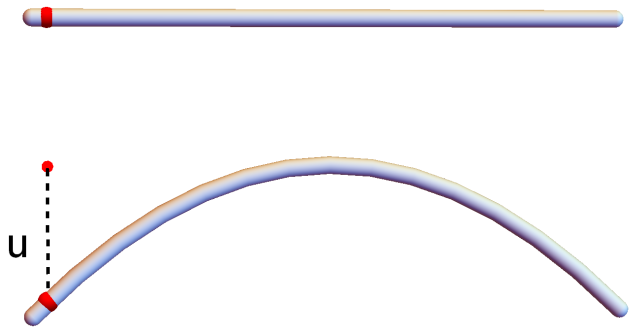

Figure A.0.1: An object small in two dimensions: the thin rod. The lower figure is the deflected version of the upper rod. The red point near the left end of the rod is displaced significantly from its original position. The displacement vector $\vec{u}$ is large, such that the last term in Eq. 2.1.2 cannot be neglected.